Commun. Comput. Phys.
doi: 10.4208/cicp.OA-2021-0169

Vol. **32**, No. 1, pp. 189-221
July 2022

An Adaptive Moving Mesh Method for the Five-Equation Model

Yaguang Gu[1,2], Dongmi Luo[3], Zhen Gao[1,*] and Yibing Chen[3]

[1] *School of Mathematical Sciences, Ocean University of China, Qingdao, Shandong, China.*
[2] *College of Oceanic and Atmospheric Sciences, Ocean University of China, Qingdao, Shandong, China.*
[3] *Institute of Applied Physics and Computational Mathematics, Beijing, China.*

Received 13 August 2021; Accepted (in revised version) 2 April 2022

Abstract. The five-equation model of multi-component flows has been attracting much attention among researchers during the past twenty years for its potential in the study of the multi-component flows. In this paper, we employ a second order finite volume method with minmod limiter in spatial discretization, which preserves local extrema of certain physical quantities and is thus capable of simulating challenging test problems without introducing non-physical oscillations. Moreover, to improve the numerical resolution of the solutions, the adaptive moving mesh strategy proposed in [Huazhong Tang, Tao Tang, Adaptive mesh methods for one- and two-dimensional hyperbolic conservation laws, SINUM, 41: 487-515, 2003] is applied. Furthermore, the proposed method can be proved to be capable of preserving the velocity and pressure when they are initially constant, which is essential in material interface capturing. Finally, several classical numerical examples demonstrate the effectiveness and robustness of the proposed method.

AMS subject classifications: 35L65, 65M08, 76T10

Key words: Multi-component flows, five-equation model, finite volume method, minmod limiter, adaptive moving mesh method, stiffened gas EOS.

1 Introduction

Numerical study of the five equation model of two-component flows, proposed in [1], has been attracting much attention during the past twenty years, due to its wide range of applications in inertial confinement fusion, underwater explosion, shock bubble dynamics,

*Corresponding author. *Email addresses:* guyaguang@ouc.edu.cn (Y. Gu), dongmiluo@stu.xmu.edu.cn (D. Luo), zhengao@ouc.edu.cn (Z. Gao), chen_yibing@iapcm.ac.cn (Y. Chen)

and so on. Much work can be seen in the literature, such as finite volume method with high order weighted essentially non-oscillatory (WENO) reconstructions [5], discontinuous Galerkin (DG) approaches [4, 28, 29], high order finite difference alternative WENO (AWENO) method [11]. Other auxiliary techniques for the five-equation model such as bound- and positivity-preserving limiters can be found in [4, 12, 29, 44]. These studies cover the fluids with ideal, stiffened, and Mie-Grüneisen equations of state (EOS).

In capturing physical structures of the fluid, such as rarefaction waves, contact discontinuities and shocks, a core issue is that the proposed method should not produce spurious oscillations. TVD (total variation diminishing) reconstruction is an effective way of remedying this issue [23, 39]. One such possibility is to use linear reconstruction with minmod slope limiter, as it is easy to implement in one and higher dimensions. The minmod limiter compares the candidate slopes and selects the one with minimum magnitude if they have same sign, otherwise it returns zero slope. Modified by the minmod limiter, linear reconstructions provide approximations of the related physical quantities at cell interfaces, such that their local extrema are well preserved. As a result, spurious oscillations are not produced. However, a limitation of this approach is that it achieves only second order of accuracy, and solutions would be relatively dissipative, compared to those computed by high order methods. To remedy this limitation, a straightforward idea is to use adaptive mesh methods, such as adaptive mesh refinement method [17–19, 24, 26, 40], or adaptive moving mesh method [13–15, 20, 22, 25, 27, 38, 43, 46] which will be considered in this paper. There are mainly two categories of the adaptive moving mesh methods. The one is that a new distribution of the grid points is computed prior to solution evolution step at each time step, and the solution is then evolved directly to the next time level on the new mesh grids. Related studies can be seen in [20, 27]. The other one is to separate the adaptive moving mesh step from the solution evolution step, which is adopted in this paper. In this approach, the solutions are updated by repeating three steps: 1) evolve the solution to the next time step, 2) update the distribution of the grid points based on the solutions to be adapted, 3) update the solutions onto the newly computed mesh grids, where the latter two steps form the adaptive moving mesh strategy.

To solve compressible multi-component flows, there are mainly two types of approaches: sharp interface methods and diffusive interface methods. The sharp interface methods include Lagrangian or Lagrangian-Eulerian methods [16, 42], front tracking methods [9], level set methods [2, 30], ghost fluid methods [8, 48], and so on. In these methods, the material interface is resolved prior to the discretization strategy designed for fluids separated by the material interface. The diffusive interface methods allow a small amount of artificial transition zone at material interface, due to unavoidable numerical diffusion. If the physical law is well defined in this diffusive zone, the existing classical methods for single-component model, such as Euler equations, would be activated. Readers may refer to [34] for a comprehensive review of diffusive interface methods.

A notable feature of the model is that the velocity and pressure should remain unchanged during computation once they are initially constants, which is referred to as

E-property. As is pointed out in the literature [1, 32], the preservation of this feature is critical in avoiding presence of spurious oscillations when a numerical discretization is designed. Besides, since the fluids are mixed near material interface and the numerical method is designed directly based on the mixture of fluids, preservation of the E-property becomes the principal issue. Therefore, the corresponding analysis will be systematically addressed.

In this paper, a finite volume diffusive interface method is introduced for the five-equation model. To improve numerical resolution of the solutions, the adaptive mesh method is also employed on quadrilateral mesh. We follow [14, 15, 38] to update the mesh grids and solutions. Besides, with the help of the adaptive mesh method, the proposed method is numerically demonstrated to be effective and robust by simulating some challenging problems with ideal and stiffened fluids equations of state (EOS). The corresponding numerical resolution of solutions is also improved.

The rest of this paper is organized as follows. The five-equation model is introduced in Section 2. We then describe second order finite volume discretizations in one- and two-dimensions and prove the E-property in Section 3. Moreover, the adaptive moving mesh method is revisited in Section 4. Finally, numerical examples demonstrate the effectiveness and robustness of our approach in Section 5.

2 Five-equation model

We consider in this paper the five-equation model [1,47], which has potentials in the simulation of immiscible two-material compressible flows, such as gas-gas and gas-liquid interactions. In one dimension, the five-equation model contains four conservative equations and one advection equation:

$$\begin{aligned}
&\frac{\partial(z_1\rho_1)}{\partial t}+\frac{\partial(z_1\rho_1 u)}{\partial x}=0,\\
&\frac{\partial(z_2\rho_2)}{\partial t}+\frac{\partial(z_2\rho_2 u)}{\partial x}=0,\\
&\frac{\partial(\rho u)}{\partial t}+\frac{\partial(\rho u^2+p)}{\partial x}=0,\\
&\frac{\partial E}{\partial t}+\frac{\partial((E+p)u)}{\partial x}=0,
\end{aligned} \tag{2.1}$$

$$\frac{\partial z_1}{\partial t}+u\frac{\partial z_1}{\partial x}=0, \tag{2.2}$$

where ρ_j is the density of the j-th component; u is the velocity; p is the pressure; $E=\frac{1}{2}\rho u^2+\rho e$ is the total energy of mixture; z_j is the volume fraction of the j-th component, satisfying $\sum_j z_j=1$. Besides, the first two conservative variables, i.e. $z_1\rho_1$ and $z_2\rho_2$, are partial densities of the first and the second components, respectively. Their sum is the density of mixture, i.e. $\rho=z_1\rho_1+z_2\rho_2$.

We notice that for ease of designing at least second order finite volume methods, the following equation is suggested instead of (2.2):

$$\frac{\partial z_1}{\partial t}+\frac{\partial z_1 u}{\partial x}=z_1\frac{\partial u}{\partial x}. \tag{2.3}$$

The reason will be stated in Section 3; see also detailed explanations in [5, 21]. It now allows us to combine (2.1) and (2.3), and to rewrite them in a compact form:

$$\frac{\partial Q}{\partial t}+\frac{\partial F(Q)}{\partial x}=S(Q), \tag{2.4}$$

where

$$Q=(\tilde{Q}^T,z_1)^T=\begin{bmatrix} z_1\rho_1 \\ z_2\rho_2 \\ \rho u \\ E \\ z_1 \end{bmatrix},\quad F(Q)=\begin{bmatrix} z_1\rho_1 u \\ z_2\rho_2 u \\ \rho u^2+p \\ (E+p)u \\ z_1 u \end{bmatrix},\quad S(Q)=\begin{bmatrix} 0 \\ 0 \\ 0 \\ 0 \\ z_1\frac{\partial u}{\partial x} \end{bmatrix}.$$

In this paper, the system (2.4) is solved for all the one-dimensional problems.

Similarly in two dimensions, the governing equations which are considered under the finite volume framework proposed in this paper read:

$$\frac{\partial Q}{\partial t}+\nabla\cdot\mathbf{F}(Q)=S(Q), \tag{2.5}$$

where $\nabla=(\partial_x,\partial_y)^T$, $\mathbf{F}(Q)=(F(Q),G(Q))$ and

$$F(Q)=\begin{bmatrix} z_1\rho_1 u \\ z_2\rho_2 u \\ \rho u^2+p \\ \rho uv \\ (E+p)u \\ z_1 u \end{bmatrix},\quad G(Q)=\begin{bmatrix} z_1\rho_1 v \\ z_2\rho_2 v \\ \rho uv \\ \rho v^2+p \\ (E+p)v \\ z_1 v \end{bmatrix},\quad S(Q)=\begin{bmatrix} 0 \\ 0 \\ 0 \\ 0 \\ 0 \\ z_1\nabla\cdot\mathbf{u} \end{bmatrix},$$

where $\mathbf{u}=(u,v)^T$.

In this study, the ideal and stiffened fluids are considered where the equations of state are of the form

$$p_j=(\gamma_j-1)\rho_j e_j-\gamma_j\pi_{\infty,j},\quad j=1,2,$$

where $\gamma_j>1$ is the specific heat ratio, and $\pi_{\infty,j}\geq 0$ is the reference pressure (where $\pi_{\infty,j}=0$ for ideal gases and $\pi_{\infty,j}>0$ for stiffened fluids). In those cells where different materials are mixed, the isobaric assumption is adopted [1], and one may refer to [1, 11, 29] and derive the equation of state for mixture:

$$p=(\gamma-1)\rho e-\gamma\pi_\infty, \tag{2.6}$$

where γ and π_∞ are computed by

$$\frac{1}{\gamma-1}=\sum_j\frac{z_j}{\gamma_j-1},\quad \frac{\gamma\pi_\infty}{\gamma-1}=\sum_j\frac{z_j\gamma_j\pi_{\infty,j}}{\gamma_j-1}. \tag{2.7}$$

3 Spatial and temporal discretizations

3.1 Spatial discretization in one dimension

Let $\Omega_p=[x_a,x_b]$ be the physical domain, and let $x_a=x_{\frac{1}{2}}<x_{\frac{3}{2}}<\cdots<x_{N_x+\frac{1}{2}}=x_b$ be a partition which forms control volumes (or cells) $A_i=(x_{i-\frac{1}{2}},x_{i+\frac{1}{2}})$. We denote the size and barycenter of the i-th volume by $\Delta x_i=x_{i+\frac{1}{2}}-x_{i-\frac{1}{2}}$ and $x_i=\frac{1}{2}(x_{i-\frac{1}{2}}+x_{i+\frac{1}{2}})$, respectively.

Integrating (2.4) on each control volume and dividing on both sides by Δx_i gives standard finite volume discretization of (2.4), i.e.

$$\frac{\partial\bar{Q}_i}{\partial t}=\frac{1}{\Delta x_i}(F_{i-\frac{1}{2}}-F_{i+\frac{1}{2}})+\bar{S}_i, \tag{3.1}$$

where

$$\bar{Q}_i=\frac{1}{\Delta x_i}\int_{A_i}Q(x,t)\,dx, \tag{3.2}$$

$$\bar{S}_i=\frac{1}{\Delta x_i}\int_{A_i}S(Q)(x,t)\,dx. \tag{3.3}$$

Note that only the fifth entry of $\bar{S}_i$ is non-zero.

Our goal in this paper is to design a second order finite volume scheme, which requires linear reconstructions in each control volume. Meanwhile, the reconstruction should preserve the E-property. To this end, we perform linear reconstructions based on primitive variables $V=(z_1\rho_1,z_2\rho_2,u,p,z_1)^T$:

$$V_i(x)=\bar{V}_i+\mathbf{r}_i(x-x_i), \tag{3.4}$$

where $\mathbf{r}_i$ is the vector of approximated slopes of the primitive variables in the control volume A_i, and $\bar{V}_i=(\overline{z_1\rho_1},\overline{z_2\rho_2},\bar{u},\bar{p},\bar{z}_1)_i^T$ with $\bar{u}$ and $\bar{p}$ being directly computed from the cell averages of conservative variables. Switches between the conservative and primitive variables do not affect the order of accuracy since the cell average of a linear polynomial is exactly the same as the function value at the barycenter. Moreover, in order to remove non-physical oscillations near discontinuities, the TVD minmod limiter [23] is adopted for the slope vector $\mathbf{r}_i$, i.e. for each entry $r_i^{(k)}$, $k=1,2,\cdots,5$,

$$r_i^{(k)}=\text{minmod}\left(\frac{\bar{V}_i^{(k)}-\bar{V}_{i-1}^{(k)}}{x_i-x_{i-1}},\frac{\bar{V}_i^{(k)}-\bar{V}_{i+1}^{(k)}}{x_i-x_{i+1}}\right), \tag{3.5}$$

where

$$\text{minmod}(a,b)=\begin{cases}a, & \text{if } |a|<|b| \text{ and } ab>0,\\ b, & \text{if } |b|<|a| \text{ and } ab>0,\\ 0, & \text{otherwise.}\end{cases} \tag{3.6}$$

Next, estimates of V at the cell interfaces $x_{i+\frac{1}{2}}$ and $x_{i-\frac{1}{2}}$, denoted by $V^-_{i+\frac{1}{2}}$ and $V^+_{i-\frac{1}{2}}$ respectively, are computed by

$$V^-_{i+\frac{1}{2}} = \bar{V}_i + \mathbf{r}_i(x_{i+\frac{1}{2}} - x_i), \quad V^+_{i-\frac{1}{2}} = \bar{V}_i + \mathbf{r}_i(x_{i-\frac{1}{2}} - x_i). \tag{3.7}$$

Finally, these estimates are converted back to those of the conservative variables at the cell interfaces.

The remaining two tasks are to estimate 1) the fluxes at the cell interfaces $x_{i\pm\frac{1}{2}}$ and 2) the cell averages of S in (3.3). For the flux term, one may replace the exact flux by a consistent and Lipschitz continuous numerical flux, such as the classical Lax-Friedrichs numerical flux. For the source term $\bar{S}$, an estimate of the fifth entry of the source term, denoted by $\bar{s}^{(5)}_i$, is

$$\bar{s}^{(5)}_i = \frac{\bar{z}_i(u_{i+\frac{1}{2}} - u_{i-\frac{1}{2}})}{\Delta x_i}, \tag{3.8}$$

where $z \triangleq z_1$, and $u_{i\pm\frac{1}{2}}$ are approximations to the velocity u at the cell interfaces $x = x_{i\pm\frac{1}{2}}$, respectively. If the volume fraction is smooth, the above mid-point formula provides a second order approximation to $\bar{s}^{(5)}_i$. When there is an interface separating two different components, an interpretation stated in [21] is that this discretization is exact far away from the interface between two components, while it is of at most first order of accuracy at the discontinuity of z_1. These discussions would well explain why we compute (2.3) instead of (2.2). Afterwards, one can observe that (3.8) is a discretization of $\bar{z}_i u_x$ with constant coefficient $\bar{z}_i$, which allows us to absorb the source terms into the flux terms and define a spatial discretization operator $\mathcal{L}$ as

$$\mathcal{L}(Q_i) := \frac{1}{\Delta x_i}(\hat{f}_{i-\frac{1}{2}} - \hat{f}_{i+\frac{1}{2}}), \tag{3.9}$$

where $\hat{f}_{i+\frac{1}{2}}$ is an approximation to $F_{i+\frac{1}{2}} - \tilde{S}_{i+\frac{1}{2}}$, with $\tilde{S}_{i+\frac{1}{2}} := (0,0,0,0,\bar{z}_i u_{i+\frac{1}{2}})^T$. As a result, the fifth entry of $\hat{f}_{i+\frac{1}{2}}$ becomes $[(z-\bar{z}_i)u]|_{x_{i+\frac{1}{2}}}$, which implies that the estimate of the velocity u in the flux and source term of the fifth equation would be consistent, which is essential in preservation of the E-property. In practical computation, the newly defined "flux" term $\hat{f}_{i+\frac{1}{2}}$ is approximated by the Lax-Friedrichs numerical flux

$$\hat{f}_{i+\frac{1}{2}} = \frac{1}{2}\left[\left(F(Q^+_{i+\frac{1}{2}}) - \tilde{S}^+_{i+\frac{1}{2}}\right) + \left(F(Q^-_{i+\frac{1}{2}}) - \tilde{S}^-_{i+\frac{1}{2}}\right)\right] - \frac{\alpha_{i+\frac{1}{2}}}{2}\left(Q^+_{i+\frac{1}{2}} - Q^-_{i+\frac{1}{2}}\right), \tag{3.10}$$

where $\tilde{S}^\pm_{i+\frac{1}{2}} = (0,0,0,0,\bar{z}_i u^\pm_{i+\frac{1}{2}})^T$ and $\alpha_{i+\frac{1}{2}} = \max_{i-1\le j\le i+2}\{|u|_j + c_j\}$, where $c = \sqrt{\gamma(p+\pi_\infty)/\rho}$ is the sound speed.

3.2 Spatial discretization in two dimensions

Let $\Omega_p=[x_a,x_b]\times[y_a,y_b]$ be the physical domain in two dimensions, and let

$$\{A_{i,j}\,|\,A_{i,j}\subset\Omega_p,\ 1\le i\le N_x,\ 1\le j\le N_y\} \tag{3.11}$$

be a structured quadrilateral partition of the physical domain, i.e. the vertices of $A_{i,j}$ are $(x_{i-\frac{1}{2}},y_{j+\frac{1}{2}})$, $(x_{i-\frac{1}{2}},y_{j-\frac{1}{2}})$, $(x_{i+\frac{1}{2}},y_{j-\frac{1}{2}})$, and $(x_{i+\frac{1}{2}},y_{j+\frac{1}{2}})$. We denote the barycenter and area of the (i,j)-th volume by $\mathbf{x}_{i,j}=(x_{i,j},y_{i,j})$ and $|A_{i,j}|$, respectively.

Integrating (2.5) on each control volume and applying the divergence theorem, one can obtain a spatial finite volume discretization of (2.5) as follows:

$$\frac{\partial\bar{Q}_{ij}}{\partial t}=-\frac{1}{|A_{i,j}|}\sum_{\ell=1}^{4}d_{i,j}^{\ell}(\mathbf{F}_{i,j}^{\ell}-\tilde{\mathbf{S}}_{i,j}^{\ell})\cdot\mathbf{n}_{i,j}^{\ell}, \tag{3.12}$$

where $\bar{Q}_{i,j}$ is the cell average of Q on $A_{i,j}$, i.e.

$$\bar{Q}_{i,j}=\frac{1}{|A_{i,j}|}\int_{A_{i,j}}Q(\mathbf{x})\,d\mathbf{x};$$

$d_{i,j}^{\ell}$ is the length of the ℓ-th edge of $A_{i,j}$; $\mathbf{n}_{i,j}^{\ell}=(n_{i,j}^{\ell,x},n_{i,j}^{\ell,y})$ is the unit outer normal to the ℓ-th edge of $A_{i,j}$; $\mathbf{F}_{i,j}^{\ell}$ is the flux vector at the mid-point of the ℓ-th edge of $A_{i,j}$, and the source vector $\tilde{\mathbf{S}}_{i,j}^{\ell}$ at the same point is of the form $\tilde{\mathbf{S}}_{i,j}^{\ell}=(\tilde{S}_{i,j}^{\ell,u},\tilde{S}_{i,j}^{\ell,v})$ with $\tilde{S}_{i,j}^{\ell,u}=(0,0,0,0,0,\bar{z}_{i,j}u_{i,j}^{\ell})^T$ and $\tilde{S}_{i,j}^{\ell,v}=(0,0,0,0,0,\bar{z}_{ij}v_{i,j}^{\ell})^T$. Note that in (3.12) we have used similar technique as in (3.8) for the source term.

To achieve second order of accuracy, a linear polynomial is reconstructed on $A_{i,j}$ such that it preserves the cell average on $A_{i,j}$. In order to preserve the E-property, the reconstruction would also be performed on the primitive variables. Let $V=(z_1\rho_1,z_2\rho_2,u,v,p,z_1)^T$ be the vector of the primitive variables. The reconstruction patch contains four extra volumes which share a common edge with $A_{i,j}$, i.e. $A_{i-1,j}$, $A_{i+1,j}$, $A_{i,j-1}$, and $A_{i,j+1}$. Then four candidate linear polynomials can be reconstructed on $\{A_{i-1,j},A_{i,j},A_{i,j+1}\}$, $\{A_{i-1,j},A_{i,j},A_{i,j-1}\}$, $\{A_{i+1,j},A_{i,j},A_{i,j+1}\}$, and $\{A_{i+1,j},A_{i,j},A_{i,j-1}\}$ respectively, such that each candidate polynomial admits cell averages on all the related volumes. Taking the stencil $\{A_{i-1,j},A_{i,j},A_{i,j+1}\}$ for example, we are aiming to reconstruct for each primitive variable a linear polynomial which is of the form $V_{i,j}^{(k)}(\mathbf{x})=\bar{V}_{i,j}^{(k)}+(r_{i,j}^{x,(k)},r_{i,j}^{y,(k)})^T\cdot(\mathbf{x}-\mathbf{x}_{i,j})$, $k=1,2,\cdots,6$, with $r_{i,j}^{x,(k)}$ and $r_{i,j}^{y,(k)}$ the approximated slopes in x- and y-directions respectively, such that

$$\frac{1}{|A_{i,j}|}\int_{A_{i,j}}V_{i,j}^{(k)}(\mathbf{x})\,d\mathbf{x}=\bar{V}_{i,j}^{(k)},\quad \frac{1}{|A_{i-1,j}|}\int_{A_{i-1,j}}V_{i,j}^{(k)}(\mathbf{x})\,d\mathbf{x}=\bar{V}_{i-1,j}^{(k)},$$
$$\frac{1}{|A_{i,j+1}|}\int_{A_{i,j+1}}V_{i,j}^{(k)}(\mathbf{x})\,d\mathbf{x}=\bar{V}_{i,j+1}^{(k)}.$$

The first constraint is naturally satisfied since the cell average is exactly the same as the function value at the barycenter. The other two constraints form a linear system which is easy to solve. Once these four linear polynomials are reconstructed, the minmod limiter is adopted to modify the x- and y-directional slopes, such that local extrema are preserved and non-physical oscillations are thus suppressed. Afterwards, the velocity $(u_{i,j}^{\ell,-},v_{i,j}^{\ell,-})^T$ and the conservative variables $Q_{i,j}^{\ell,-}$ are estimated at each mid-point of the ℓ-th edge of $A_{i,j}$. The estimates at the same point in adjacent volume is denoted by $(u_{i,j}^{\ell,+},v_{i,j}^{\ell,+})$ and $Q_{i,j}^{\ell,+}$.

Finally, we define the spatial discretization operator, still denoted by $\mathcal{L}$, as

$$\mathcal{L}(\bar{Q}_{i,j})=-\frac{1}{|A_{i,j}|}\sum_{\ell=1}^{4}d_{i,j}^{\ell}\hat{f}_{i,j}^{\ell}, \tag{3.13}$$

where the flux $\hat{f}_{i,j}^{\ell}=(\mathbf{F}_{i,j}^{\ell}-\tilde{\mathbf{S}}_{i,j}^{\ell})\cdot\mathbf{n}_{i,j}^{\ell}$ is approximated by the Lax-Friedrichs numerical flux

$$\hat{f}_{i,j}^{\ell}=\frac{1}{2}\left[\left(\mathbf{F}(Q_{i,j}^{\ell,+})-\tilde{\mathbf{S}}_{i,j}^{\ell,+}\right)+\left(\mathbf{F}(Q_{i,j}^{\ell,-})-\tilde{\mathbf{S}}_{i,j}^{\ell,-}\right)\right]\cdot\mathbf{n}_{i,j}^{\ell}-\frac{\alpha_{i,j}^{\ell}}{2}\left(Q_{i,j}^{\ell,+}-Q_{i,j}^{\ell,-}\right). \tag{3.14}$$

where the parameter $\alpha_{i,j}^{\ell}$ is computed by $\alpha_{i,j}^{\ell}=\max\{|\mathbf{u}_{i,j}\cdot\mathbf{n}_{i,j}^{\ell}|+c_{i,j}\}$, where "max" is taken over local reconstruction volumes.

3.3 Temporal discretization

Let $\mathcal{T}$ be an one-step time integration operator defined by

$$\mathcal{T}(Q_i)=Q_i+\Delta t\mathcal{L}(Q_i), \tag{3.15}$$

where the time step Δt is defined as

$$\Delta t=\begin{cases}\text{CFL}\min_i\left\{\frac{\Delta x_i}{|u_i|+c_i}\right\}, & \text{in 1D},\\ \text{CFL}\min_{i,j}\left\{\frac{\text{dist}(\mathbf{x}_{i,j},\partial A_{i,j})}{\max_\ell\{\mathbf{u}_{i,j}\cdot\mathbf{n}_\ell\}+c_{i,j}},\right\}, & \text{in 2D}.\end{cases} \tag{3.16}$$

In this paper, the second order Runge-Kutta (RK) method [35] is adopted for temporal discretization:

$$\begin{aligned}&Q^*=\mathcal{T}(\bar{Q}^n),\\ &\bar{Q}^{n+1}=\frac{1}{2}(\bar{Q}^n+\mathcal{T}(Q^*)).\end{aligned} \tag{3.17}$$

3.4 Equilibriums of the velocity and pressure in moving interface problems

An important feature of the five equation model is that equilibrium states of the velocity and pressure are preserved when they are initially constant, which is referred to as E-property. A discretization method, therefore, is required to preserve this E-property numerically. In this section, we are going to prove that the proposed finite volume scheme meets the requirements. For simplicity, we use in this section w_i to denote the cell average of w on A_i in one dimension, and use $w_{i,j}$ to denote the cell average of w on $A_{i,j}$ in two dimensions, where w can be chosen as any physical quantity. One may also regard w_i and $w_{i,j}$ as function values at the barycenters x_i and $\mathbf{x}_{i,j}$, since the unknowns are approximated by piecewise linear polynomials.

We may pause for a moment, and define some notations for the proofs.

(1) The temporal jump $\Delta^k[f]=f^{k+1}-f^k$. An easy derivation gives $\Delta^k[fg]=f^{k+1}\Delta^k[g]+g^k\Delta^k[f]$.

(2) Lax-Friedrichs flux related operators $\delta_1[f]=f^++f^-$ and $\delta_2[f]=f^+-f^-$.

Now, we state our main results as follows. We first prove the following lemmas.

Lemma 3.1. *Let the velocity and pressure be two constants, and let Q_i^k, $Q_{i-\frac{1}{2}}^{\pm}$ and $Q_{i+\frac{1}{2}}^{\pm}$ be vectors of the conservative variables in one dimension such that*

$$u(Q_i^k)=u(Q_{i-\frac{1}{2}}^-)=u(Q_{i-\frac{1}{2}}^+)=u(Q_{i+\frac{1}{2}}^-)=u(Q_{i+\frac{1}{2}}^+)=u,$$
$$p(Q_i^k)=p(Q_{i-\frac{1}{2}}^-)=p(Q_{i-\frac{1}{2}}^+)=p(Q_{i+\frac{1}{2}}^-)=p(Q_{i+\frac{1}{2}}^+)=p.$$

Then the one-step solution update

$$Q_i^{k+1}=Q_i^k+\left(c_1Q_i^k+c_2\delta_1[Q]_{i-\frac{1}{2}}+c_3\delta_2[Q]_{i-\frac{1}{2}}+c_4\delta_1[Q]_{i+\frac{1}{2}}+c_5\delta_2[Q]_{i+\frac{1}{2}}\right) \tag{3.18}$$

with constant parameters $c_1,\cdots,c_5$, preserves the same velocity and pressure, i.e. $u(Q_i^{k+1})=u$ and $p(Q_i^{k+1})=p$.

Proof. We rewrite (3.18) as

$$\Delta^k[Q_i]=c_1Q_i^k+c_2\delta_1[Q]_{i-\frac{1}{2}}+c_3\delta_2[Q]_{i-\frac{1}{2}}+c_4\delta_1[Q]_{i+\frac{1}{2}}+c_5\delta_2[Q]_{i+\frac{1}{2}}, \tag{3.19}$$

and prove that $\Delta^k[u_i]=0$ and $\Delta^k[p_i]=0$.

To prove the equilibrium of the velocity, one may add the first two equations up to obtain

$$\Delta^k[\rho_i]=c_1\rho_i^k+c_2\delta_1[\rho]_{i-\frac{1}{2}}+c_3\delta_2[\rho]_{i-\frac{1}{2}}+c_4\delta_1[\rho]_{i+\frac{1}{2}}+c_5\delta_2[\rho]_{i+\frac{1}{2}},$$

and then derives from the third equation that

$$\begin{aligned}\rho_i^{k+1}\Delta^k[u_i]+u\Delta^k[\rho_i]&=\Delta^k[(\rho u)_i]\\&=c_1(\rho u)_i^k+c_2\delta_1[\rho u]_{i-\frac{1}{2}}+c_3\delta_2[\rho u]_{i-\frac{1}{2}}+c_4\delta_1[\rho u]_{i+\frac{1}{2}}+c_5\delta_2[\rho u]_{i+\frac{1}{2}}\\&=u\Delta^k[\rho_i],\end{aligned}$$

which implies, with positive density ρ_i^{k+1}, that $\Delta^k[u_i]=0$.

To prove the equilibrium of the pressure, we first prove the following four properties.

(i) $\Delta^k[(z_j)_i]=c_1(z_j)_i^k+c_2\delta_1[z_j]_{i-\frac{1}{2}}+c_3\delta_2[z_j]_{i-\frac{1}{2}}+c_4\delta_1[z_j]_{i+\frac{1}{2}}+c_5\delta_2[z_j]_{i+\frac{1}{2}}$, $j=1,2$.

The equality for $j=1$ is transparent since it is exactly the fifth equation in (3.19). When $j=2$, the equality can be derived by replacing z_2 by $1-z_1$ and using the linearity of the operator Δ^k.

(ii) $\Delta^k[\Gamma_i]=c_1\Gamma_i^k+c_2\delta_1[\Gamma]_{i-\frac{1}{2}}+c_3\delta_2[\Gamma]_{i-\frac{1}{2}}+c_4\delta_1[\Gamma]_{i+\frac{1}{2}}+c_5\delta_2[\Gamma]_{i+\frac{1}{2}}$, where $\Gamma:=\frac{1}{\gamma-1}=\sum_j\frac{z_j}{\gamma_j-1}$.

Since γ_j, $j=1,2$, are constants for the ideal and stiffened fluids, one has by the definition of Γ that

$$\begin{aligned}\Delta^k[\Gamma_i]&=\Delta^k\left[\left(\sum_j\frac{z_j}{\gamma_j-1}\right)_i\right]=\sum_j\frac{\Delta^k[(z_j)_i]}{\gamma_j-1}\\&=\sum_j\frac{1}{\gamma_j-1}\left(c_1(z_j)_i^k+c_2\delta_1[z_j]_{i-\frac{1}{2}}+c_3\delta_2[z_j]_{i-\frac{1}{2}}+c_4\delta_1[z_j]_{i+\frac{1}{2}}+c_5\delta_2[z_j]_{i+\frac{1}{2}}\right)\\&=c_1\Gamma_i^k+c_2\delta_1[\Gamma]_{i-\frac{1}{2}}+c_3\delta_2[\Gamma]_{i-\frac{1}{2}}+c_4\delta_1[\Gamma]_{i+\frac{1}{2}}+c_5\delta_2[\Gamma]_{i+\frac{1}{2}}.\end{aligned}$$

(iii) $\Delta^k[(\Pi_\infty)_i]=c_1(\Pi_\infty)_i^k+c_2\delta_1[\Pi_\infty]_{i-\frac{1}{2}}+c_3\delta_2[\Pi_\infty]_{i-\frac{1}{2}}+c_4\delta_1[\Pi_\infty]_{i+\frac{1}{2}}+c_5\delta_2[\Pi_\infty]_{i+\frac{1}{2}}$, where $\Pi_\infty:=\frac{\gamma\pi_\infty}{\gamma-1}=\sum_j\frac{z_j\gamma_j\pi_{\infty,j}}{\gamma_j-1}$.

The proof is similar to that of (ii), and is thus omitted.

(iv) $\Delta^k[(\rho e)_i]=c_1(\rho e)_i^k+c_2\delta_1[\rho e]_{i-\frac{1}{2}}+c_3\delta_2[\rho e]_{i-\frac{1}{2}}+c_4\delta_1[\rho e]_{i+\frac{1}{2}}+c_5\delta_2[\rho e]_{i+\frac{1}{2}}$.

The fourth equation in (3.19) reads

$$\Delta^k[E_i]=c_1E_i^k+c_2\delta_1[E]_{i-\frac{1}{2}}+c_3\delta_2[E]_{i-\frac{1}{2}}+c_4\delta_1[E]_{i+\frac{1}{2}}+c_5\delta_2[E]_{i+\frac{1}{2}}.$$

Since $E=\frac{1}{2}\rho u^2+\rho e$, one has

$$\begin{aligned}\Delta^k[E_i]=&c_1\left(\frac{1}{2}\rho u^2+\rho e\right)_i^k+c_2\delta_1\left[\frac{1}{2}\rho u^2+\rho e\right]_{i-\frac{1}{2}}+c_3\delta_2\left[\frac{1}{2}\rho u^2+\rho e\right]_{i-\frac{1}{2}}\\&+c_4\delta_1\left[\frac{1}{2}\rho u^2+\rho e\right]_{i+\frac{1}{2}}+c_5\delta_2\left[\frac{1}{2}\rho u^2+\rho e\right]_{i+\frac{1}{2}}\\=&c_1\left(\frac{1}{2}\rho u^2\right)_i^k+c_2\delta_1\left[\frac{1}{2}\rho u^2\right]_{i-\frac{1}{2}}+c_3\delta_2\left[\frac{1}{2}\rho u^2\right]_{i-\frac{1}{2}}+c_4\delta_1\left[\frac{1}{2}\rho u^2\right]_{i+\frac{1}{2}}+c_5\delta_2\left[\frac{1}{2}\rho u^2\right]_{i+\frac{1}{2}}\\&+c_1(\rho e)_i^k+c_2\delta_1[\rho e]_{i-\frac{1}{2}}+c_3\delta_2[\rho e]_{i-\frac{1}{2}}+c_4\delta_1[\rho e]_{i+\frac{1}{2}}+c_5\delta_2[\rho e]_{i+\frac{1}{2}}.\end{aligned}$$

Then

$$\begin{aligned}\Delta^k[(\rho e)_i] &= \Delta^k\left[E_i - \left(\frac{1}{2}\rho u^2\right)_i\right] \\ &= c_1(\rho e)_i^k + c_2\delta_1[\rho e]_{i-\frac{1}{2}} + c_3\delta_2[\rho e]_{i-\frac{1}{2}} + c_4\delta_1[\rho e]_{i+\frac{1}{2}} + c_5\delta_2[\rho e]_{i+\frac{1}{2}},\end{aligned}$$

where we have used that

$$\begin{aligned}&\Delta^k\left[\left(\frac{1}{2}\rho u^2\right)_i\right] = \frac{1}{2}u^2\Delta^k[\rho_i] \\ &= \frac{1}{2}u^2\left(c_1\rho_i^k + c_2\delta_1[\rho]_{i-\frac{1}{2}} + c_3\delta_2[\rho]_{i-\frac{1}{2}} + c_4\delta_1[\rho]_{i+\frac{1}{2}} + c_5\delta_2[\rho]_{i+\frac{1}{2}}\right) \\ &= c_1\left(\frac{1}{2}\rho u^2\right)_i^k + c_2\delta_1\left[\frac{1}{2}\rho u^2\right]_{i-\frac{1}{2}} + c_3\delta_2\left[\frac{1}{2}\rho u^2\right]_{i-\frac{1}{2}} + c_4\delta_1\left[\frac{1}{2}\rho u^2\right]_{i+\frac{1}{2}} + c_5\delta_2\left[\frac{1}{2}\rho u^2\right]_{i+\frac{1}{2}}.\end{aligned}$$

Based on the above analysis, one can use the relation $\rho e = \Gamma p + \Pi_\infty$ to derive that

$$\begin{aligned}&\Delta^k[(\Gamma p)_i] + \Delta^k[(\Pi_\infty)_i] \\ &= \Delta^k[(\rho e)_i] \\ &= c_1(\rho e)_i^k + c_2\delta_1[\rho e]_{i-\frac{1}{2}} + c_3\delta_2[\rho e]_{i-\frac{1}{2}} + c_4\delta_1[\rho e]_{i+\frac{1}{2}} + c_5\delta_2[\rho e]_{i+\frac{1}{2}} \\ &= c_1(\Gamma p)_i^k + c_2\delta_1[\Gamma p]_{i-\frac{1}{2}} + c_3\delta_2[\Gamma p]_{i-\frac{1}{2}} + c_4\delta_1[\Gamma p]_{i+\frac{1}{2}} + c_5\delta_2[\Gamma p]_{i+\frac{1}{2}} \\ &\quad + c_1(\Pi_\infty)_i^k + c_2\delta_1[\Pi_\infty]_{i-\frac{1}{2}} + c_3\delta_2[\Pi_\infty]_{i-\frac{1}{2}} + c_4\delta_1[\Pi_\infty]_{i+\frac{1}{2}} + c_5\delta_2[\Pi_\infty]_{i+\frac{1}{2}} \\ &= p\Delta^k[\Gamma_i] + \Delta^k[(\Pi_\infty)_i].\end{aligned}$$

Therefore, $\Delta^k[(\Gamma p)_i] = p\Delta^k[\Gamma_i]$, from which one can prove that $\Delta[p_i] = 0$. □

Remark 3.1. In Lemma 3.1, we generalize the analysis studied in [11]. This lemma will be used to proved that the finite volume discretization (3.9) and the solution update formula (4.3) in moving mesh method which is presented in Section 4 preserves the E-property.

Lemma 3.2. *For the one-dimensional model, let Q_1 and Q_2 be two vectors of the conservative variables, such that $u(Q_1) = u(Q_2) = u$ and $p(Q_1) = p(Q_2) = p$. Then for all convex combinations $Q = aQ_1 + bQ_2$, with $0 \le a,b \le 1$, $a+b=1$,*

$$u(Q) = u, \quad p(Q) = p.$$

Proof. Without loss of generality, we denote $Q_1 = (q_1^1, q_2^1, (q_1^1+q_2^1)u, q_4^1, q_5^1)^T$ and $Q_2 = (q_1^2, q_2^2, (q_1^2+q_2^2)u, q_4^2, q_5^2)^T$, due to the requirement that $u(Q_1) = u(Q_2) = u$. Then

$$Q = aQ_1 + bQ_2 = (aq_1^1 + bq_1^2, aq_2^1 + bq_2^2, \left[a(q_1^1+q_2^1) + b(q_1^2+q_2^2)\right]u, aq_4^1 + bq_4^2, aq_5^1 + bq_5^2)^T.$$

The derivation of $u(Q)=u$ is simple, since

$$u(Q)=\frac{\rho u(Q)}{\rho(Q)}=\frac{\left[a(q_1^1+q_2^1)+b(q_1^2+q_2^2)\right]u}{aq_1^1+bq_1^2+aq_2^1+bq_2^2}=u.$$

To prove $p(Q)=p$, one may first use (2.6) and (2.7) for $p(Q_1)$ and $p(Q_2)$ to obtain

$$\begin{aligned}
\frac{p(Q_1)}{\gamma(Q_1)-1}&=\frac{p}{\gamma(Q_1)-1}=q_4^1-\frac{1}{2}(q_1^1+q_2^1)u^2-\left(\frac{q_5^1\gamma_1\pi_{\infty,1}}{\gamma_1-1}+\frac{(1-q_5^1)\gamma_2\pi_{\infty,2}}{\gamma_2-1}\right),\\
\frac{p(Q_2)}{\gamma(Q_2)-1}&=\frac{p}{\gamma(Q_2)-1}=q_4^2-\frac{1}{2}(q_1^2+q_2^2)u^2-\left(\frac{q_5^2\gamma_1\pi_{\infty,1}}{\gamma_1-1}+\frac{(1-q_5^2)\gamma_2\pi_{\infty,2}}{\gamma_2-1}\right),
\end{aligned}$$

and then derive $p(Q)$ by using (2.6), (2.7) and the above two equations:

$$\begin{aligned}
\frac{p(Q)}{\gamma(Q)-1}&=(aq_4^1+bq_4^2)-\frac{1}{2}\left[a(q_1^1+q_2^1)+b(q_1^2+q_2^2)\right]u^2\\
&\quad-\frac{(aq_5^1+bq_5^2)\gamma_1\pi_{\infty,1}}{\gamma_1-1}-\frac{(1-aq_5^1-bq_5^2)\gamma_2\pi_{\infty,2}}{\gamma_2-1}\\
&=\left(\frac{a}{\gamma(Q_1)-1}+\frac{b}{\gamma(Q_2)-1}\right)p\\
&=\left(\frac{aq_5^1}{\gamma_1-1}+\frac{a(1-q_5^1)}{\gamma_2-1}+\frac{bq_5^2}{\gamma_1-1}+\frac{b(1-q_5^2)}{\gamma_2-1}\right)p=\frac{p}{\gamma(Q)-1},
\end{aligned}$$

which implies, with $\frac{1}{\gamma(Q)-1}>0$, that $p(Q)=p$. □

Now we are ready to state our main result in one dimension.

Theorem 3.1. *Suppose that $u_i^0=u=$ constant and $p_i^0=p=$ constant over the whole domain, then the one-dimensional finite volume discretization, which consists of* (3.9), (3.10) *and* (3.17), *produces $u_i^n=u$, $p_i^n=p$ at any future time.*

Proof. It suffices for us to prove that $u(Q_i^{n+1})=u$ and $p(Q_i^{n+1})=p$, provided $u(Q_i^n)=u$ and $p(Q_i^n)=p$ for all index i.

Let $\tilde{Q}=(\widetilde{z_1\rho_1},\widetilde{z_2\rho_2},\tilde{\rho}u,\tilde{E},\tilde{z}_1)^T$ denote the vector of conservative variables after linear reconstruction procedure at $t=t^n$, where $\tilde{\rho}=\widetilde{z_1\rho_1}+\widetilde{z_2\rho_2}$ and $\tilde{E}=\widetilde{\rho e}+\frac{1}{2}\tilde{\rho}u^2$ with $\widetilde{\rho e}$ being

computed by (2.6) using $\tilde{z}_1$ and p. Then the numerical flux $\hat{f}_{i\pm\frac{1}{2}}$ can be represented by $\tilde{Q}_i$:

$$\begin{aligned}\hat{f}_{i\pm\frac{1}{2}} &= \frac{1}{2}\left[\left(F(Q^+_{i\pm\frac{1}{2}})-\tilde{S}^+_{i\pm\frac{1}{2}}\right)+\left(F(Q^-_{i\pm\frac{1}{2}})-\tilde{S}^-_{i\pm\frac{1}{2}}\right)-\alpha_{i\pm\frac{1}{2}}\left(Q^+_{i\pm\frac{1}{2}}-Q^-_{i\pm\frac{1}{2}}\right)\right],\\ &= \frac{1}{2}\left\{u\begin{bmatrix}\widetilde{z_1\rho_1}\\ \widetilde{z_2\rho_2}\\ \tilde{\rho}u\\ \tilde{E}\\ \tilde{z}_1\end{bmatrix}^+_{i\pm\frac{1}{2}}+u\begin{bmatrix}\widetilde{z_1\rho_1}\\ \widetilde{z_2\rho_2}\\ \tilde{\rho}u\\ \tilde{E}\\ \tilde{z}_1\end{bmatrix}^-_{i\pm\frac{1}{2}}-\alpha_{i\pm\frac{1}{2}}\left(\begin{bmatrix}\widetilde{z_1\rho_1}\\ \widetilde{z_2\rho_2}\\ \tilde{\rho}u\\ \tilde{E}\\ \tilde{z}_1\end{bmatrix}^+_{i\pm\frac{1}{2}}-\begin{bmatrix}\widetilde{z_1\rho_1}\\ \widetilde{z_2\rho_2}\\ \tilde{\rho}u\\ \tilde{E}\\ \tilde{z}_1\end{bmatrix}^-_{i\pm\frac{1}{2}}\right)\right\}+C,\\ &= C+\frac{u}{2}\delta_1[\tilde{Q}]_{i\pm\frac{1}{2}}-\frac{\alpha_{i\pm\frac{1}{2}}}{2}\delta_2[\tilde{Q}]_{i\pm\frac{1}{2}},\end{aligned}$$

where $C=(0,0,p,pu,u(\bar{z}_1)_i)^T$. The first step of the Runge-Kutta method can thus be rewritten as

$$Q^*_i=\bar{Q}^n_i+\frac{\Delta t}{\Delta x}\left(\frac{u}{2}\delta_1[\tilde{Q}]_{i-\frac{1}{2}}-\frac{\alpha_{i-\frac{1}{2}}}{2}\delta_2[\tilde{Q}]_{i-\frac{1}{2}}-\frac{u}{2}\delta_1[\tilde{Q}]_{i+\frac{1}{2}}+\frac{\alpha_{i+\frac{1}{2}}}{2}\delta_2[\tilde{Q}]_{i+\frac{1}{2}}\right). \tag{3.20}$$

By Lemma 3.1, one can prove that $u(Q^*_i)=u$ and $p(Q^*_i)=p$. In the second step of the Runge-Kutta method, $\mathcal{T}(Q^*)$ preserves the same velocity and pressure as well. Note that Q^n and $\mathcal{T}(Q^*)$ are added up by a convex combination, one has by Lemma 3.2 that $u(\bar{Q}^{n+1}_i)=u$ and $p(\bar{Q}^{n+1}_i)=p$. □

Next, we describe how to prove E-property in two dimensions. If the velocity u, v and the pressure p are constant over the whole physical domain, the finite volume discretization operator (3.13) can then be written as

$$\mathcal{L}(\bar{Q}_{i,j})=-\frac{1}{|A_{i,j}|}\sum_{\ell=1}^{4}\frac{d_\ell}{2}\left(n^x_\ell u\delta_1[Q]_\ell+n^y_\ell v\delta_1[Q]_\ell-\alpha_\ell\delta_2[Q]_\ell\right),$$

where we have used that for any quadrilateral $\sum_{\ell=1}^4 d_\ell\mathbf{n}_\ell=\mathbf{0}$.

Based on these observations, we list below two lemmas and one theorem for two dimensions without proofs, as they can be proved by mimicking Lemma 3.1, Lemma 3.2 and Theorem 3.1.

Lemma 3.3. *Let the velocity u, v and the pressure p be constants, and let $Q^k_{i,j}$, Q^-_ℓ and Q^+_ℓ be vectors of the conservative variables in two dimensions such that*

$$\begin{aligned}u(Q^k_{i,j})&=u(Q^-_\ell)=u(Q^+_\ell)=u,\\ v(Q^k_{i,j})&=v(Q^-_\ell)=v(Q^+_\ell)=v,\\ p(Q^k_{i,j})&=p(Q^-_\ell)=p(Q^+_\ell)=p.\end{aligned}$$

Then the one-step solution update formula

$$Q_{i,j}^{k+1}=Q_{i,j}^{k}+\sum_{\ell=1}^{4}\left(c_\ell^1 Q_{i,j}^{k+1}+c_\ell^2\delta_1[Q]_l+c_\ell^3\delta_3[Q]_\ell\right) \tag{3.21}$$

with constant parameters $c_\ell^1,\cdots,c_\ell^3$, *preserves the same velocity and pressure, i.e.* $u(Q_{i,j}^{k+1})=u$, $v(Q_{i,j}^{k+1})=v$ *and* $p(Q_{i,j}^{k+1})=p$.

Lemma 3.4. *For the two-dimensional model, let* Q_1 *and* Q_2 *be two vectors of the conservative variables in two dimensions, such that* $u(Q_1)=u(Q_2)=u$, $v(Q_1)=v(Q_2)=v$ *and* $p(Q_1)=p(Q_2)=p$. *Then for all convex combinations* $Q=aQ_1+bQ_2$, *with* $0\le a,b\le 1$, $a+b=1$,

$$u(Q)=u,\quad v(Q)=v,\quad p(Q)=p.$$

Theorem 3.2. *Suppose that* $u_{i,j}^0=u=$*constant*, $v_{i,j}^0=v=$*constant and* $p_{i,j}^0=p=$*constant over the whole physical domain. The two-dimensional finite volume discretization, which consists of* (3.13), (3.14) *and* (3.17), *produces* $u_{i,j}^n=u$, $v_{i,j}^n=v$ *and* $p_{i,j}^n=p$ *at any future time.*

4 Adaptive moving mesh method

In this section, we revisit the adaptive moving mesh method proposed in [38]. Meanwhile, we will show that a use of the adaptive moving mesh method does not destroy the E-property.

4.1 One-dimensional adaptive moving mesh method

Let Ω_c be the computational domain, and let $0=\xi_{\frac{1}{2}}<\xi_{\frac{3}{2}}<\cdots<\xi_{N_x+\frac{1}{2}}=1$ be a uniform partition. A surjective mapping between the coordinates x and ξ is determined by minimizing a functional of the following form:

$$E(x)=\frac{1}{2}\int_{\Omega_c}\omega(x_\xi)^2\,d\xi,$$

where $\omega=\omega(Q)>0$ is a monitor function depending on the underlying solutions to be adapted and will be specified in each test case in Section 5. The Euler-Lagrange equation associated with the above functional reads

$$(\omega x_\xi)_\xi=0, \tag{4.1}$$

whose solution forms a new distribution of the mesh grids denoted by $\tilde{x}_{i+\frac{1}{2}}$, $i=0,\cdots,N_x$. It is also required that $\tilde{x}_{\frac{1}{2}}=x_{\frac{1}{2}}$ and $\tilde{x}_{N_x+\frac{1}{2}}=x_{N_x+\frac{1}{2}}$ since they are at the physical boundaries.

To solve (4.1), the Gauss-Seidel-type iteration is suggested by the authors in [38]:

$$\omega_{i+1}(x_{i+\frac{3}{2}}-\tilde{x}_{i+\frac{1}{2}})-\omega_i(\tilde{x}_{i+\frac{1}{2}}-\tilde{x}_{i-\frac{1}{2}})=0,\quad 1\le i\le N_x-1, \tag{4.2}$$

where ω_i is computed by a spatial smoothing of the volume-wise monitor functions in the following way, avoiding a singular mesh distribution and/or large approximation errors near the regions where the gradient of the solution is very large [38]

$$\omega_i=\frac{1}{4}(\omega(\bar{Q}_{i-1})+2\omega(\bar{Q}_i)+\omega(\bar{Q}_{i+1})).$$

It has been proved in [38] that $\tilde{x}_{i-\frac{1}{2}}<\tilde{x}_{i+\frac{1}{2}}$ for all i; in other words, no distortion of the mesh is generated.

Then, one could use the cell averages and the linearly reconstructed values on the previous mesh to obtain new cell averages on the newly updated mesh:

$$\bar{\tilde{Q}}_i=\frac{\Delta x_i}{\Delta\tilde{x}_i}\bar{Q}_i-\frac{1}{\Delta\tilde{x}_i}\Big((cQ)_{i+\frac{1}{2}}-(cQ)_{i-\frac{1}{2}}\Big), \tag{4.3}$$

where $\Delta x_i=x_{i+\frac{1}{2}}-x_{i-\frac{1}{2}}$, $\Delta\tilde{x}_i=\tilde{x}_{i+\frac{1}{2}}-\tilde{x}_{i-\frac{1}{2}}$, $c_{i\pm\frac{1}{2}}=x_{i\pm\frac{1}{2}}-\tilde{x}_{i\pm\frac{1}{2}}$, and the flux terms $(cQ)_{i\pm\frac{1}{2}}$ are defined by

$$(cQ)_{i\pm\frac{1}{2}}=\frac{1}{2}c_{i\pm\frac{1}{2}}\Big(Q^+_{i\pm\frac{1}{2}}+Q^-_{i\pm\frac{1}{2}}\Big)-\frac{1}{2}|c_{i\pm\frac{1}{2}}|\Big(Q^+_{i\pm\frac{1}{2}}-Q^-_{i\pm\frac{1}{2}}\Big), \tag{4.4}$$

which achieves second order of accuracy. It is easy to prove that conservations of the conservative variables are guaranteed in the sense that $\sum_i\Delta\tilde{x}_i\bar{\tilde{Q}}_i=\sum_i\Delta x_i\bar{Q}_i$.

Note that the mesh algorithm (4.2) only produces small displacements of the grid points. In order to obtain a satisfactory redistribution of the grid points, we perform five full Gauss-Seidel-type iterations which is suggested in [38].

We enclose this sub-section by pointing out that the solution update procedure (4.3) does not destroy the E-property. Observe that $\Delta\tilde{x}=\Delta x-(c_{i+\frac{1}{2}}-c_{i-\frac{1}{2}})$. The solution update procedure (4.3) can be written as

$$\bar{\tilde{Q}}_i=\bar{Q}_i+\left(\frac{\Delta x_i-\Delta\tilde{x}_i}{\Delta\tilde{x}_i}\bar{Q}_i+\frac{c_{i-\frac{1}{2}}}{2\Delta\tilde{x}_i}\delta_1[Q]_{i-\frac{1}{2}}-\frac{|c_{i-\frac{1}{2}}|}{2\Delta\tilde{x}_i}\delta_2[Q]_{i-\frac{1}{2}}-\frac{c_{i+\frac{1}{2}}}{2\Delta\tilde{x}_i}\delta_1[Q]_{i+\frac{1}{2}}+\frac{|c_{i+\frac{1}{2}}|}{2\Delta\tilde{x}_i}\delta_2[Q]_{i+\frac{1}{2}}\right).$$

Consequently, one can see by Lemma 3.1 that the E-property is not destroyed after a use of the adaptive moving mesh method.

4.2 Two-dimensional adaptive moving mesh method

Let $\Omega_c=[0,1]\times[0,1]$ be the computational domain in two dimensions, and let ξ and η be the coordinates. The new distribution of the coordinates on the physical domain is defined by minimizing the following functional:

$$E(x)=\frac{1}{2}\int_{\Omega_c}\Big((\widetilde{\nabla}x)^TG_x\widetilde{\nabla}x+(\widetilde{\nabla}y)^TG_y\widetilde{\nabla}y\Big)\,d\xi d\eta,$$

where $\widetilde{\nabla}=(\partial_{\xi},\partial_{\eta})^T$, and the monitor functions G_x and G_y are 2×2 symmetric positive definite matrices. One may solve for x and y the Euler-Lagrange equations associated with the above functional:

$$\widetilde{\nabla}\cdot(G_x\widetilde{\nabla}x)=0,\quad \widetilde{\nabla}\cdot(G_y\widetilde{\nabla}y)=0. \tag{4.5}$$

There are much work on discussions of the choice of the monitor functions G_x and G_y. The simplest choice, for example, is to set $G_x=G_y=\omega I$ [43]. Another simple choice studied in [14,38] is $G_x=G_y=\mathrm{diag}(\omega_{\xi},\omega_{\eta})$, which is more flexible than the previous one, and will degenerate to the previous one when $\omega_{\xi}=\omega_{\eta}$. Therefore, $G_x=G_y=\mathrm{diag}(\omega_{\xi},\omega_{\eta})$ is adopted in this paper. A good design of the monitor functions is essential in the mesh redistribution procedure, and affects the behaviour of the numerical solutions. Concrete choices of the monitor functions will be given in each test case in Section 5.

To solve for the new distribution of the interior nodes $\tilde{\mathbf{x}}_{i+\frac{1}{2},j+\frac{1}{2}}=(\tilde{x}_{i+\frac{1}{2},j+\frac{1}{2}},\tilde{y}_{i+\frac{1}{2},j+\frac{1}{2}})^T$, one can apply conservative central differences to the Euler-Lagrange equations (4.5), and solve by Gauss-Seidel-type iterations as follows:

$$\begin{aligned}&(\omega_{\xi})_{i+1,j+\frac{1}{2}}\left(\mathbf{x}_{i+\frac{3}{2},j+\frac{1}{2}}-\tilde{\mathbf{x}}_{i+\frac{1}{2},j+\frac{1}{2}}\right)-(\omega_{\xi})_{i,j+\frac{1}{2}}\left(\tilde{\mathbf{x}}_{i+\frac{1}{2},j+\frac{1}{2}}-\tilde{\mathbf{x}}_{i-\frac{1}{2},j+\frac{1}{2}}\right)\\&+(\omega_{\eta})_{i+\frac{1}{2},j+1}\left(\mathbf{x}_{i+\frac{1}{2},j+\frac{3}{2}}-\tilde{\mathbf{x}}_{i+\frac{1}{2},j+\frac{1}{2}}\right)-(\omega_{\eta})_{i+\frac{1}{2},j}\left(\tilde{\mathbf{x}}_{i+\frac{1}{2},j+\frac{1}{2}}-\tilde{\mathbf{x}}_{i+\frac{1}{2},j-\frac{1}{2}}\right)=0,\end{aligned} \tag{4.6}$$

where

$$\begin{aligned}&(\omega_{\xi})_{i,j+\frac{1}{2}}=\frac{1}{2}\left(\omega_{\xi}(Q_{i,j})+\omega_{\xi}(Q_{i,j+1})\right),\quad (\omega_{\xi})_{i+1,j+\frac{1}{2}}=\frac{1}{2}\left(\omega_{\xi}(Q_{i+1,j})+\omega_{\xi}(Q_{i+1,j+1})\right),\\&(\omega_{\eta})_{i+\frac{1}{2},j}=\frac{1}{2}\left(\omega_{\eta}(Q_{i,j})+\omega_{\eta}(Q_{i+1,j})\right),\quad (\omega_{\eta})_{i+\frac{1}{2},j+1}=\frac{1}{2}\left(\omega_{\eta}(Q_{i,j+1})+\omega_{\eta}(Q_{i+1,j+1})\right).\end{aligned}$$

Again, to avoid a very singular mesh distribution, the following smoothing procedure is suggested for the monitor functions 2-3 times; see also [14].

$$\begin{aligned}(\omega_{\xi/\eta})_{i,j}=&\frac{1}{4}(\omega_{\xi/\eta})_{i,j}+\frac{1}{8}\left[(\omega_{\xi/\eta})_{i-1,j}+(\omega_{\xi/\eta})_{i+1,j}+(\omega_{\xi/\eta})_{i,j-1}+(\omega_{\xi/\eta})_{i,j+1}\right]\\&+\frac{1}{16}\left[(\omega_{\xi/\eta})_{i-1,j-1}+(\omega_{\xi/\eta})_{i-1,j+1}+(\omega_{\xi/\eta})_{i+1,j-1}+(\omega_{\xi/\eta})_{i+1,j+1}\right].\end{aligned}$$

Besides, the nodes on the physical boundaries (except the four corner ones) also need to be redistributed, such that discontinuities near boundaries at the initial and/or any future time can be well captured. This is done by setting

$$\tilde{x}_{i+\frac{1}{2},\frac{1}{2}}=x_{i+\frac{1}{2},\frac{1}{2}}+\left(\tilde{x}_{i+\frac{1}{2},\frac{3}{2}}-x_{i+\frac{1}{2},\frac{3}{2}}\right) \tag{4.7}$$

for all the interior nodes on the lower boundary of the physical domain. The nodes on the other three boundaries can be modified similarly.

Once a new distribution of the grid points is obtained, the solution on the new mesh needs to be updated. Denote $\mathbf{c}(c^x,c^y)=\mathbf{x}(x,y)-\tilde{\mathbf{x}}(\tilde{x},\tilde{y})$. Based on a perturbation analysis [38], the solution on the new mesh is interpolated from that on the old mesh by

$$\int_{\tilde{A}_{i,j}}\tilde{Q}(\tilde{\mathbf{x}})\,d\tilde{\mathbf{x}}\approx\int_{A_{i,j}}Q(\mathbf{x})\,d\mathbf{x}-\int_{A_{i,j}}\nabla\cdot(\mathbf{c}Q)\,d\mathbf{x}.$$

To achieve second order of accuracy, the third integral is approximated by mid-point rule, which leads to the following solution update formula:

$$|\tilde{A}_{i,j}|\bar{\tilde{Q}}_{i,j}=|A_{i,j}|\bar{Q}_{i,j}-(cQ)_{i-\frac{1}{2},j}-(cQ)_{i+\frac{1}{2},j}-(cQ)_{i,j-\frac{1}{2}}-(cQ)_{i,j+\frac{1}{2}},\tag{4.8}$$

where

$$\begin{aligned}
c_{i-\frac{1}{2},j}&=d_{i-\frac{1}{2},j}\mathbf{c}_{i-\frac{1}{2},j}\cdot\mathbf{n}_{i-\frac{1}{2},j}\\
&=\frac{1}{2}\left(\begin{bmatrix}x_{i-\frac{1}{2},j+\frac{1}{2}}-\tilde{x}_{i-\frac{1}{2},j+\frac{1}{2}}\\ y_{i-\frac{1}{2},j+\frac{1}{2}}-\tilde{y}_{i-\frac{1}{2},j+\frac{1}{2}}\end{bmatrix}+\begin{bmatrix}x_{i-\frac{1}{2},j-\frac{1}{2}}-\tilde{x}_{i-\frac{1}{2},j-\frac{1}{2}}\\ y_{i-\frac{1}{2},j-\frac{1}{2}}-\tilde{y}_{i-\frac{1}{2},j-\frac{1}{2}}\end{bmatrix}\right)\cdot\begin{bmatrix}y_{i-\frac{1}{2},j-\frac{1}{2}}-y_{i-\frac{1}{2},j+\frac{1}{2}}\\ x_{i-\frac{1}{2},j+\frac{1}{2}}-x_{i-\frac{1}{2},j-\frac{1}{2}}\end{bmatrix},\\
c_{i+\frac{1}{2},j}&=d_{i+\frac{1}{2},j}\mathbf{c}_{i+\frac{1}{2},j}\cdot\mathbf{n}_{i+\frac{1}{2},j}\\
&=\frac{1}{2}\left(\begin{bmatrix}x_{i+\frac{1}{2},j-\frac{1}{2}}-\tilde{x}_{i+\frac{1}{2},j-\frac{1}{2}}\\ y_{i+\frac{1}{2},j-\frac{1}{2}}-\tilde{y}_{i+\frac{1}{2},j-\frac{1}{2}}\end{bmatrix}+\begin{bmatrix}x_{i+\frac{1}{2},j+\frac{1}{2}}-\tilde{x}_{i+\frac{1}{2},j+\frac{1}{2}}\\ y_{i+\frac{1}{2},j+\frac{1}{2}}-\tilde{y}_{i+\frac{1}{2},j+\frac{1}{2}}\end{bmatrix}\right)\cdot\begin{bmatrix}y_{i+\frac{1}{2},j+\frac{1}{2}}-y_{i+\frac{1}{2},j-\frac{1}{2}}\\ x_{i+\frac{1}{2},j-\frac{1}{2}}-x_{i+\frac{1}{2},j+\frac{1}{2}}\end{bmatrix},\\
c_{i,j-\frac{1}{2}}&=d_{i,j-\frac{1}{2}}\mathbf{c}_{i,j-\frac{1}{2}}\cdot\mathbf{n}_{i,j-\frac{1}{2}}\\
&=\frac{1}{2}\left(\begin{bmatrix}x_{i-\frac{1}{2},j-\frac{1}{2}}-\tilde{x}_{i-\frac{1}{2},j-\frac{1}{2}}\\ y_{i-\frac{1}{2},j-\frac{1}{2}}-\tilde{y}_{i-\frac{1}{2},j-\frac{1}{2}}\end{bmatrix}+\begin{bmatrix}x_{i+\frac{1}{2},j-\frac{1}{2}}-\tilde{x}_{i+\frac{1}{2},j-\frac{1}{2}}\\ y_{i+\frac{1}{2},j-\frac{1}{2}}-\tilde{y}_{i+\frac{1}{2},j-\frac{1}{2}}\end{bmatrix}\right)\cdot\begin{bmatrix}y_{i+\frac{1}{2},j-\frac{1}{2}}-y_{i-\frac{1}{2},j-\frac{1}{2}}\\ x_{i-\frac{1}{2},j-\frac{1}{2}}-x_{i+\frac{1}{2},j-\frac{1}{2}}\end{bmatrix},\\
c_{i,j+\frac{1}{2}}&=d_{i,j+\frac{1}{2}}\mathbf{c}_{i,j+\frac{1}{2}}\cdot\mathbf{n}_{i,j+\frac{1}{2}}\\
&=\frac{1}{2}\left(\begin{bmatrix}x_{i+\frac{1}{2},j+\frac{1}{2}}-\tilde{x}_{i+\frac{1}{2},j+\frac{1}{2}}\\ y_{i+\frac{1}{2},j+\frac{1}{2}}-\tilde{y}_{i+\frac{1}{2},j+\frac{1}{2}}\end{bmatrix}+\begin{bmatrix}x_{i-\frac{1}{2},j+\frac{1}{2}}-\tilde{x}_{i-\frac{1}{2},j+\frac{1}{2}}\\ y_{i-\frac{1}{2},j+\frac{1}{2}}-\tilde{y}_{i-\frac{1}{2},j+\frac{1}{2}}\end{bmatrix}\right)\cdot\begin{bmatrix}y_{i-\frac{1}{2},j+\frac{1}{2}}-y_{i+\frac{1}{2},j+\frac{1}{2}}\\ x_{i+\frac{1}{2},j+\frac{1}{2}}-x_{i-\frac{1}{2},j+\frac{1}{2}}\end{bmatrix},
\end{aligned}$$

where $d_{i\pm\frac{1}{2},j}$ and $d_{i,j\pm\frac{1}{2}}$ are the lengths of the four edges; $\mathbf{c}_{i\pm\frac{1}{2},j}$ and $\mathbf{c}_{i,j\pm\frac{1}{2}}$ are the displacements of the barycenters of the four edges. One [38] can easily prove that the conservative variables are updated in a conservative sense due to $\sum_i\sum_j|\tilde{A}_{i,j}|\bar{\tilde{Q}}_{i,j}=\sum_i\sum_j|A_{i,j}|\bar{Q}_{i,j}$. To implement (4.8), the last four terms are approximated using Lax-Friedrichs fluxes similar to those in (4.4):

$$\begin{aligned}
(cQ)_{i-\frac{1}{2},j}&=\frac{1}{2}c_{i-\frac{1}{2},j}(Q^+_{i-\frac{1}{2},j}+Q^-_{i-\frac{1}{2},j})-\frac{1}{2}|c_{i-\frac{1}{2},j}|(Q^+_{i-\frac{1}{2},j}-Q^-_{i-\frac{1}{2},j}),\\
(cQ)_{i+\frac{1}{2},j}&=\frac{1}{2}c_{i+\frac{1}{2},j}(Q^+_{i+\frac{1}{2},j}+Q^-_{i+\frac{1}{2},j})-\frac{1}{2}|c_{i+\frac{1}{2},j}|(Q^+_{i+\frac{1}{2},j}-Q^-_{i+\frac{1}{2},j}),\\
(cQ)_{i,j-\frac{1}{2}}&=\frac{1}{2}c_{i,j-\frac{1}{2}}(Q^+_{i,j-\frac{1}{2}}+Q^-_{i,j-\frac{1}{2}})-\frac{1}{2}|c_{i,j-\frac{1}{2}}|(Q^+_{i,j-\frac{1}{2}}-Q^-_{i,j-\frac{1}{2}}),\\
(cQ)_{i,j+\frac{1}{2}}&=\frac{1}{2}c_{i,j+\frac{1}{2}}(Q^+_{i,j+\frac{1}{2}}+Q^-_{i,j+\frac{1}{2}})-\frac{1}{2}|c_{i,j+\frac{1}{2}}|(Q^+_{i,j+\frac{1}{2}}-Q^-_{i,j+\frac{1}{2}}),
\end{aligned}\tag{4.9}$$

where $Q^{\pm}_{i\pm\frac{1}{2},j}$ and $Q^{\pm}_{i,j\pm\frac{1}{2}}$ are the linearly reconstructed values at the barycenters of four edges of the control volume $A_{i,j}$ introduced in Section 3. Finally, suggested by [14, 38], the two-dimensional moving mesh algorithms (4.6), (4.7) and (4.8) is repeated 3-5 times at each time level.

We enclose this sub-section by pointing out that the solution update formula (4.8) does not destroy the E-property due to Lemma 3.3.

5 Numerical experiments

In this section, robustness and effectiveness of the adaptive mesh method are illustrated by several numerical examples. We note that monitor functions play important roles in the mesh grid redistribution algorithm, and should be thus carefully designed. Based on our numerical experience, we give some suggestions on the choice of monitor functions.

- Density is the mostly concerned primitive variable, and will be used in all of the following numerical tests. In general, first order derivative would depict change of the density. But sometimes one may add second order derivative which also captures change of first order derivative of the density.
- The rarefaction wave is usually captured by introducing entropy-related variable to the monitor function once the structure of rarefaction wave is as important as other structures.
- Adaptive moving mesh methods produce as high resolution solutions as those produced by high order methods. Therefore, for those hard problems in which positivity of the sound speed is the key issue, it is reasonable to add first order derivative of $\rho e-\pi_\infty$ (as $c=\sqrt{\gamma(\gamma-1)(\rho e-\pi_\infty)/\rho}$) to the monitor function, see e.g. two-dimensional tests in this paper.
- Other physical quantities, such as volume fraction, velocity and pressure, may also help to improve quality of the mesh.

5.1 One-dimensional test cases

In this section, the adaptive moving mesh method is verified by testing the one-dimensional five-equation model. The reference solution is computed with 2000 grid points.

Accuracy test problem

In the first set of tests, convergence rate is shown by testing the following problem [10,29]:

$$\begin{aligned}&\rho_1(x,0)=\rho_2(x,0)=1.0,\quad u(x,0)=p(x,0)=1.0,\quad z_1(x,0)=0.5+0.499\sin(\pi x),\\&\gamma_1=1.4,\quad \gamma_2=1.9,\quad \pi_{\infty,1}=1.0,\quad \pi_{\infty,2}=0.0.\end{aligned}\tag{5.1}$$

Table 1: Accuracy test problem: L^1-norms of errors of the volume fraction and the convergence rate.

α \ N_x	80	160	320	640	1280
20	3.72E-02 (-)	1.26E-02 (1.56)	3.45E-03 (1.87)	8.23E-04 (2.07)	1.67E-04 (2.30)
50	3.91E-02 (-)	1.43E-02 (1.45)	4.35E-03 (1.72)	9.60E-04 (2.18)	2.10E-04 (2.19)

The problem is solved in $(0,2)$ up to $t=1.0$ with CFL $=0.95$, and the monitor function is set as

$$w=\sqrt{1+\alpha\left(\frac{(z_1)_\xi}{\max|(z_1)_\xi|}\right)^2}.$$

The volume fraction has an explicit exact solution $z_1(x,t)=0.5+0.499\sin(\pi(x-t))$, and L^1-norms of errors are shown in Table 1 for different α, One can observe that the second order convergence is well achieved.

Moving Interface Problem

In the second set of tests, the moving interface problem studied in [11, 12, 29] is used to show that the adaptive mesh method proposed in this paper preserves the E-property. The initial setup is given by

$$(\rho_1,\rho_2,u,p,\gamma,\pi,z_1)=\begin{cases}(1.0,\ 0.125,\ 1.0,\ 1.0,\ 1.4,\ 1.0,\ 1.0), & x<0,\\ (1.0,\ 0.125,\ 1.0,\ 1.0,\ 1.9,\ 0.0,\ 0.0), & x\geq 0.\end{cases} \tag{5.2}$$

The problem is solved in $(-5,5)$ with CFL $=0.95$ until $t=2.0$. Transmissive boundary conditions are used at the left and right boundaries.

The corresponding results are shown in Fig. 1, where the monitor function is chosen as

$$w=\sqrt{1+20\left(\frac{\rho_\xi}{\max|\rho_\xi|}\right)^2+20\left(\frac{\rho_{\xi\xi}}{\max|\rho_{\xi\xi}|}\right)^2}.$$

With the moving mesh method being used, the grid points are dragged towards the discontinuity, as shown at the first panel in Fig. 1. Besides, the initial discontinuities in the density and volume fraction move, with constant right-going velocity $u=1.0$, to $x=2.0$, which can be observed at the second panel in Fig. 1. We also plot L^∞-norms of errors of the velocity and pressure under different mesh resolutions at the third panel, from which one can see that the E-property is well preserved by our approach.

To show that the adaptive mesh method produces higher resolution solutions at the material interface than the ones computed on uniform mesh with $N_x=200$, we present a comparison in Fig. 2, from which one can clearly see that the contact discontinuity is better resolved by the adaptive mesh.

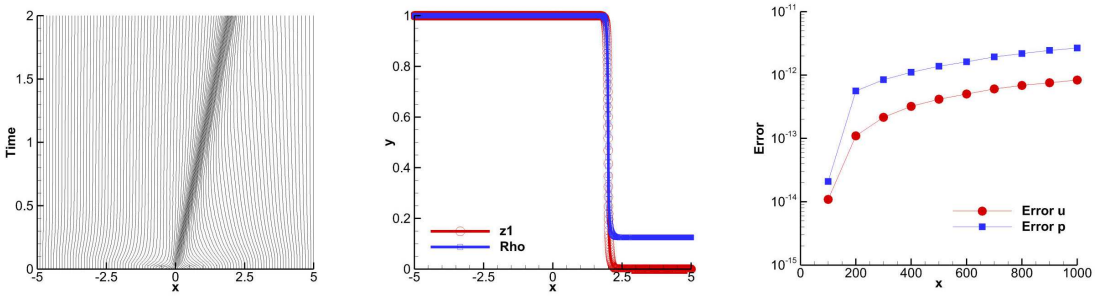

Figure 1: Moving interface problem. Left: trajectory of the mesh grids. Middle: distributions of the density and volume fraction. Right: L^∞-norms of errors of the velocity and pressure. Output time is $t=2.0$.

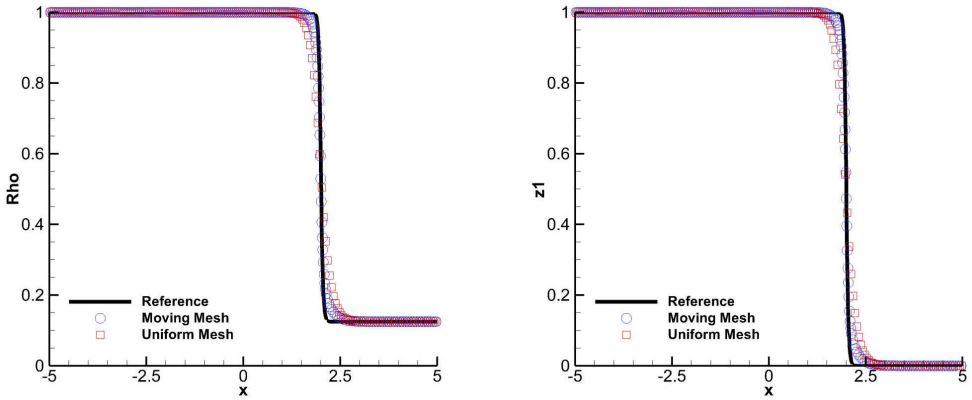

Figure 2: Distributions of the density and volume fraction for moving interface problem solved on uniform and adaptive meshes, with $N_x=200$. Output time is $t=2.0$.

Gas-liquid shock-tube problem I

In the third set of tests, numerical solutions of a classical gas-liquid shock-tube problem studied in [21,37] are shown. The initial conditions are

$$\begin{aligned}&(\rho_1,\rho_2,u,p,\gamma,\pi,z_1)\\ =&\begin{cases}(1.241,\ 0.991,\ 0.0,\ 2.753,\ \ \ \ 1.4,\ 0.0,\ \ \ 1.0), & x<0,\\ (1.241,\ 0.991,\ 0.0,\ 3.59\times10^{-4},\ 5.5,\ 1.505,\ 0.0), & x\geq 0.\end{cases}\end{aligned} \tag{5.3}$$

The problem is computed in $x\in(-5,5)$ with transmissive boundary conditions. The CFL condition number is set as 0.95, and the final time is $t=1.0$.

Numerical results are shown in Fig. 3, where the monitor function is chosen as

$$w=\sqrt{1+100\left(\frac{\rho_\xi}{\max|\rho_\xi|}\right)^2+100\left(\frac{\rho_{\xi\xi}}{\max|\rho_{\xi\xi}|}\right)^2+50\left(\frac{s_\xi}{\max|s_\xi|}\right)^2},$$

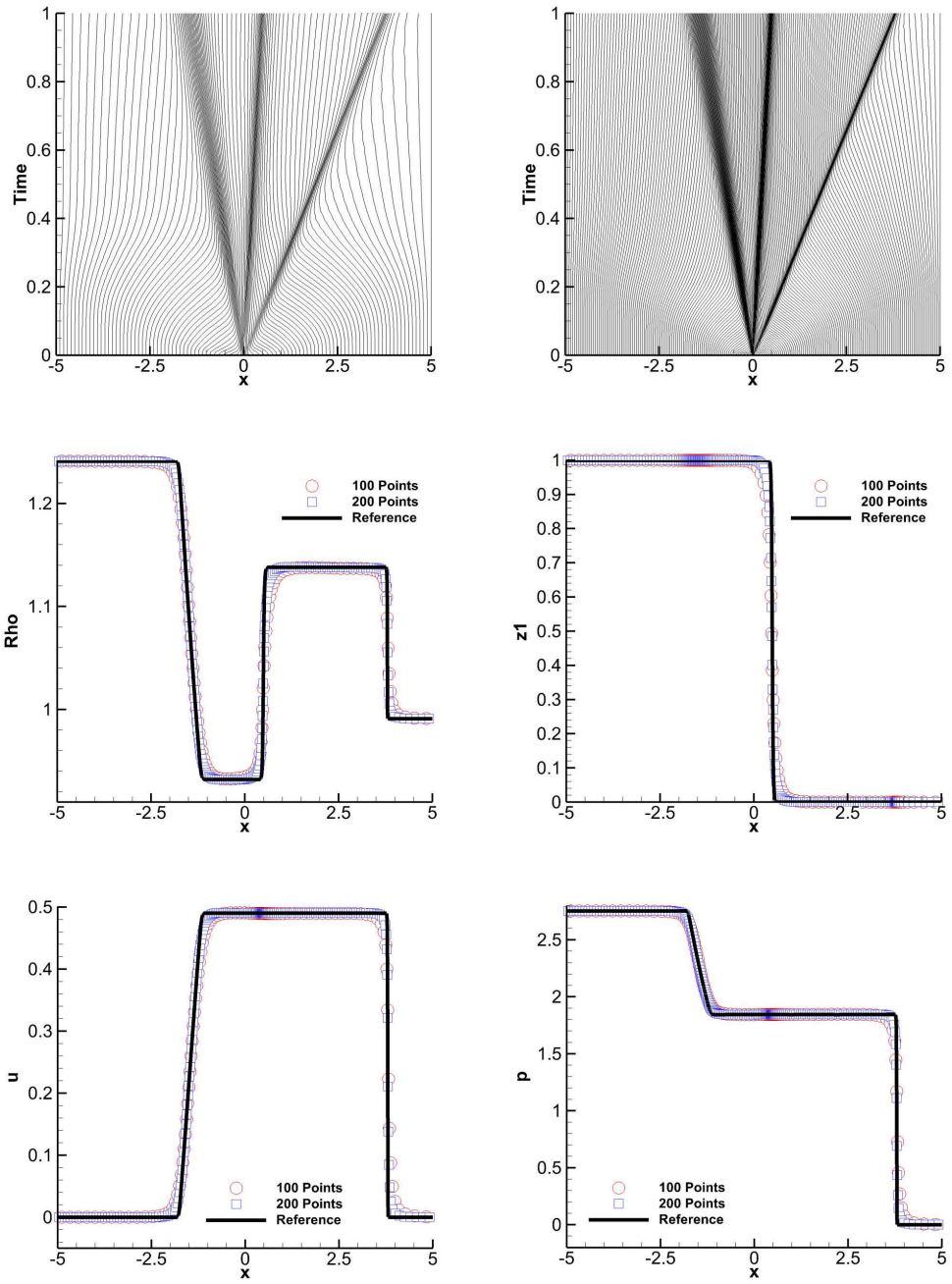

Figure 3: Distributions of the mesh grids with $N_x = 100$ (top left), and $N_x = 200$ (top right), and density (middle left), volume fraction (middle right), velocity(bottom left) and pressure(bottom right) for the gas-liquid shock-tube problem I. The final time is $t = 1.0$.

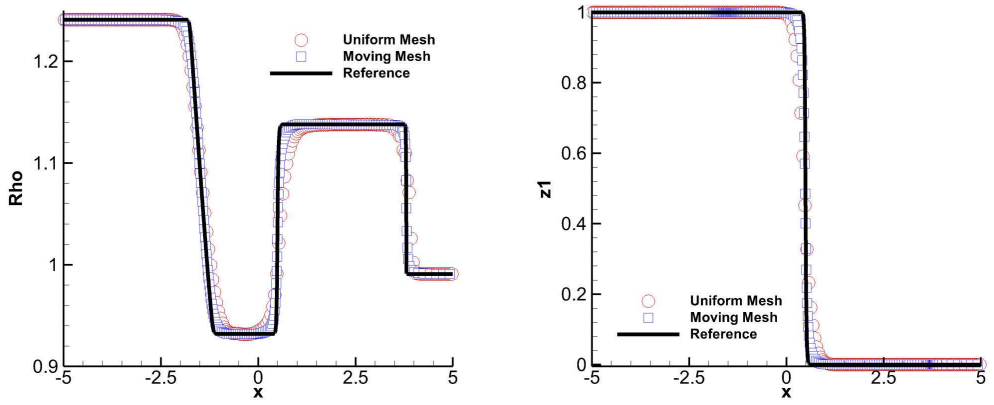

Figure 4: Distributions of the density and volume fraction for the gas-liquid shock-tube problem I on uniform and moving meshes with $N_x=200$. The final time is $t=1.0$.

where $s=\frac{p}{\rho^\gamma}$. One can see that the rarefaction wave, material interface and shock wave are perfectly resolved by the mesh. As a result, numerical solutions of the density, volume fraction, velocity and pressure match the reference ones well. Moreover, refinement study illustrates convergence of our approach.

Besides, we present in Fig. 4 a comparison test in which the problem is solved on uniform and adaptive moving meshes, with $N_x=200$. One may observe that with the help of the adaptive mesh method, the solutions become more accurate near the rarefaction wave, material interface and shock wave. In the remaining numerical tests except the first one in Section 5.2 (An air shock impacting on a helium bubble), we will not present the results on uniform mesh, and readers are convinced that the adaptive moving mesh method always produces higher resolution solutions with the same number of grid points.

Gas-liquid shock-tube problem II

In the fourth set of tests, the gas-liquid shock-tube problem studied in [3,33] is presented. The problem is computed in $x\in(0,1)$ with the following initial conditions

$$(\rho_1,\rho_2,u,p,\gamma,\pi,z_1)=\begin{cases}(5.0,\ 10^3,\ 0.0,\ 10^5,\ 1.4,\ 0.0,\ \ \ \ \ 1.0), & x<0.3,\\ (5.0,\ 10^3,\ 0.0,\ 10^9,\ 4.4,\ 6.0\times10^8,\ 0.0), & x\geq0.3.\end{cases}\tag{5.4}$$

Transmissive boundary conditions are employed at both boundaries. The CFL number is set as 0.95, and output time is $t=2.4\times10^{-4}$.

This problem is challenging for most high order numerical schemes, such as the ones studied in [3, 12, 41], due to the large discontinuities in the initial profiles of the density, pressure and π_∞. To overcome the difficulty, positivity-preserving limiters need to be used to avoid a crash of the code. The adaptive moving mesh method proposed in this paper, however, does not encounter this difficulty since new local extrema are suppressed

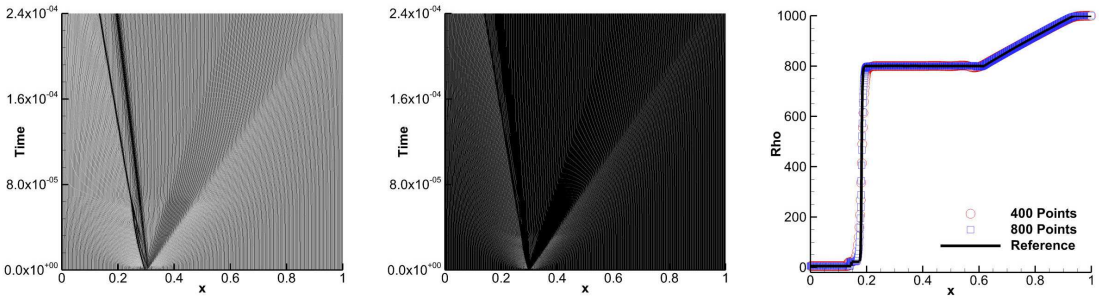

Figure 5: Distributions of the mesh grids with $N_x=400$ (left), and $N_x=800$ (middle), and density (right) for the gas-liquid shock-tube problem II. The final time is $t=2.4\times10^{-4}$.

by the minmod limiter. Although the proposed method achieves only second order of accuracy, the moving mesh method is capable of improving the numerical resolution of the solutions. Distributions of the mesh grids and density are shown in Fig. 5 where the monitor function is set as

$$w=\sqrt{1+\left(\frac{\rho_\xi}{\max|\rho_\xi|}\right)^2+100\left(\frac{u_\xi}{\max|u_\xi|}\right)^2+5\left(\frac{s_\xi}{\max|s_\xi|}\right)^2},$$

where $s=\frac{p+\pi_\infty}{\rho^\gamma}$. One can observe that distribution of the mesh grids perfectly match the basic physical structures, such as the rarefaction wave, material interface and shock wave. Besides, refinement study indicates the convergence of our algorithm, as one can see that the density gets closer to the reference solution with increasing number of grid points.

Gas-liquid shock-tube problem III

In the fifth set of tests, another challenging gas-liquid shock-tube problem studied in [28, 29] is presented. The problem is computed in $x\in(-0.2,1)$ with the following initial conditions

$$\begin{aligned}&(\rho_1,\rho_2,u,p,\gamma,\pi,z_1)\\ =&\begin{cases}(1000.0,\quad 50.0,\quad 0.0,\quad 10^9,\quad 4.4,\quad 6.0\times10^8,\quad 1.0), & x\le0.5,\\ (1000.0,\quad 50.0,\quad 0.0,\quad 10^5,\quad 1.4,\quad 0.0,\qquad\ 0.0), & x>0.5.\end{cases}\end{aligned}\tag{5.5}$$

Transmissive boundary conditions are imposed at both boundaries. The CFL number is set as 0.95, and final time is $t=2.0\times10^{-4}$.

This problem is also challenging since the pressure ratio is extremely high and the material interface and shock wave are quite close to each other. As a result, distribution of the density between the material interface and the shock wave is hard to capture. Numerical results in Fig. 6 illustrate the effectiveness of our approach, where the monitor

function is chosen to be

$$\begin{cases} \omega=\sqrt{1+\alpha_1\min\{1,\Phi_1\}^2+\alpha_2\min\{1,\Phi_2\}^2+\alpha_3\{1,\Phi_3\}^2}, \\ \Phi_1=\frac{2|\partial_{\tilde{\xi}}\phi_1|}{\max|\partial_{\tilde{\xi}}\phi_1|+\min|\partial_{\tilde{\xi}}\phi_1|}, \quad \Phi_2=\frac{2|\partial_{\tilde{\xi}\tilde{\xi}}\phi_2|}{\max|\partial_{\tilde{\xi}\tilde{\xi}}\phi_2|+\min|\partial_{\tilde{\xi}\tilde{\xi}}\phi_2|}, \quad \Phi_3=\frac{2|\partial_{\tilde{\xi}}\phi_3|}{\max|\partial_{\tilde{\xi}}\phi_3|+\min|\partial_{\tilde{\xi}}\phi_3|}, \\ \alpha_1=\alpha_2=\alpha_3=200, \\ \phi_1=\phi_2=\rho, \\ \phi_3=z_1. \end{cases}$$

Distributions of the grid points with $N_x=2000$ and its zoom-in plot in $(x,t)\in[0.3,0.6]\times[2.0\times10^{-5},6.0\times10^{-5}]$ can be seen at the top row of Fig. 6, where we output the trajectories every four grid points so that the structure can be seen clearly. One can observe that the rarefaction wave, material interface and shock wave are well resolved by the mesh. Moreover, distribution of the density with the same mesh resolution is shown at the middle row, from which we can see that the density matches the reference one [6], except that there is a slight undershoot at the material interface. This problem can be fixed by refining the mesh, as one can see that the resolution is improved when $N_x=4000$. Finally, good performances of the distributions of the velocity and pressure presented at the bottom row also demonstrate the effectiveness and robustness of the proposed method.

5.2 Two-dimensional test cases

An air shock impacting on a helium bubble

In the sixth set of tests, numerical solutions of a helium bubble impacted by an air shock are presented to demonstrate the robustness of the adaptive mesh method. The same test problem can be found in [28,31]. At the initial state, the physical quantities are

$$(\rho_1,\rho_2,u,v,p,z_1) = \begin{cases} (1.0, & 0.138, & 0.0, & 0.0, & 1.0, & 10^{-10}), & d<1.0, \\ (1.3764, & 0.138, & 0.394, & 0.0, & 1.5698, & 1.0-10^{-10}), & x<-1.2, \\ (1.0, & 0.138, & 0.0, & 0.0, & 1.0, & 1.0-10^{-10}), & \text{elsewhere}, \end{cases} \tag{5.6}$$

with $\gamma_1=1.4$, $\gamma_2=\frac{5}{3}$, $\pi_{\infty,1}=\pi_{\infty,2}=0.0$, and $d=\sqrt{x^2+y^2}$. The computational domain is $(-3,4)\times(-3,3)$. Reflective boundary conditions are imposed at the top and bottom physical boundaries, and transmissive boundary conditions are imposed elsewhere. The results are extracted at multiple output time: $t=0.5,1.0,2.0,4.0$, with CFL$=0.9$.

In the first comparison, we keep the number of the mesh grids fixed, with $N_x\times N_y=70\times60$, and test the problem on uniform and moving meshes. The monitor functions are

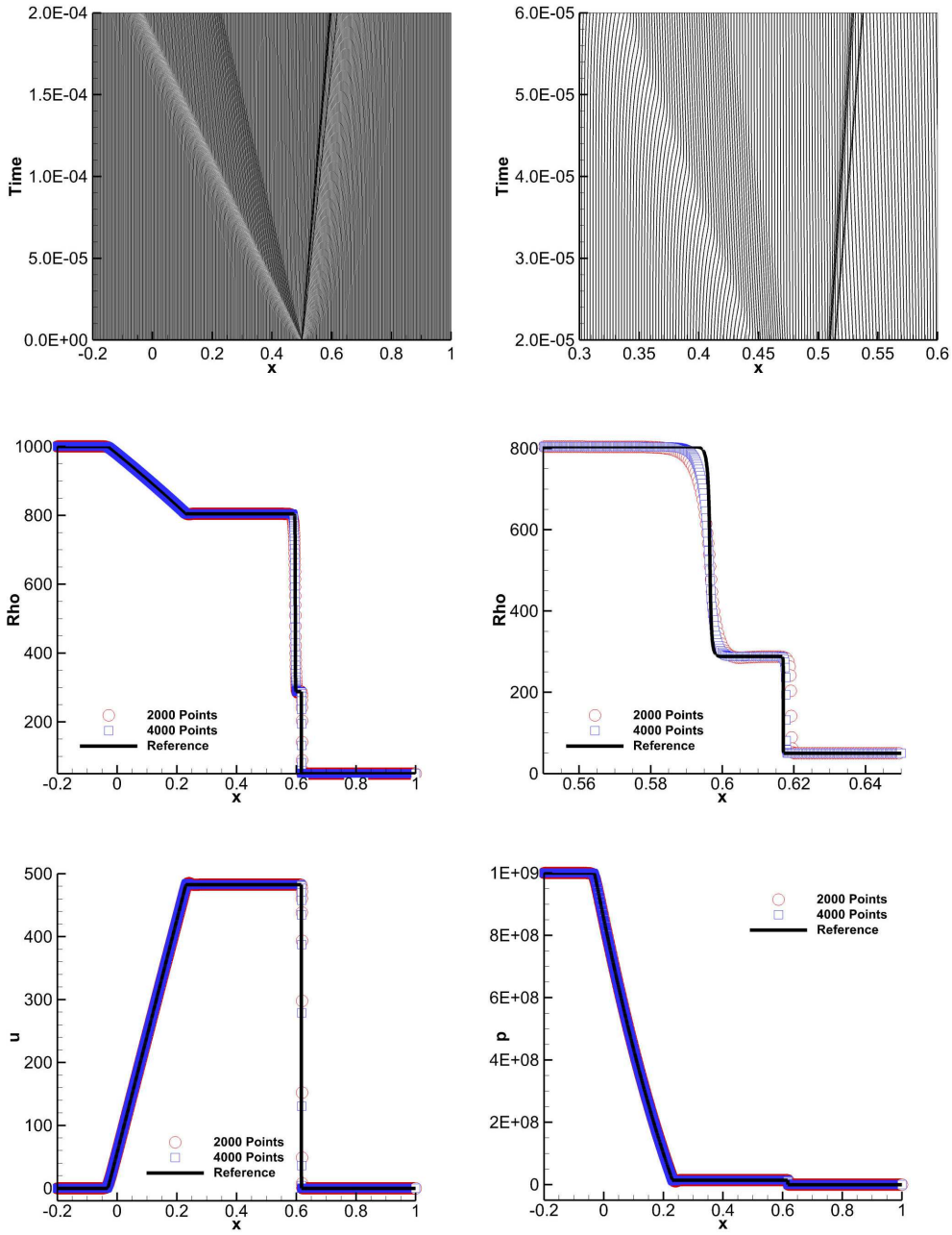

Figure 6: Gas-liquid shock-tube problem III. Top row: trajectories of the mesh grids with $N_x=2000$ on the left, and its zoom-in plot on the right. Middle row: distributions of density with $N_x=2000$ and $N_x=4000$ on the left, and its zoom-in plot on the right. Bottom row: distributions of the velocity (left) and pressure (right). The final time is $t=2.0\times10^{-4}$.

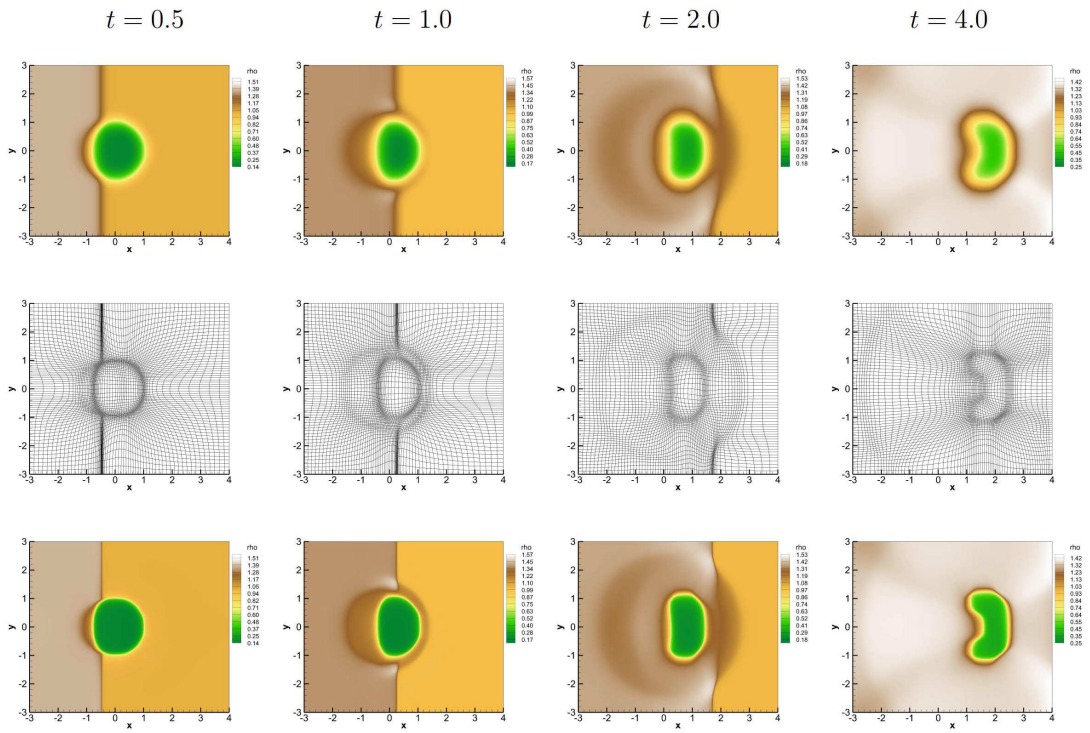

Figure 7: An air shock impacting on a helium bubble. Distributions of density computed on uniform (top) and adaptive (bottom) meshes, and distribution of mesh grids (middle), with $N_x \times N_y = 70 \times 60$, at multiple output time: $t = 0.5, 1.0, 2.0, 4.0$.

set as

$$\begin{cases} \omega_\xi(Q_{i,j}) = \sqrt{1+\alpha_1 \min\{1,\Phi_1\}^2+\alpha_2 \min\{1,\Phi_2\}^2+\alpha_3\{1,\Phi_3\}^2}, \\ \omega_\eta(Q_{i,j}) = \sqrt{1+\alpha_1 \min\{1,\Psi_1\}^2+\alpha_2 \min\{1,\Psi_2\}^2+\alpha_3\{1,\Psi_3\}^2}, \\ \alpha_1 = \alpha_2 = \alpha_3 = 200, \\ \Phi_1 = \dfrac{2|\partial_\xi \phi_1|_{i,j}}{\max_{i,j}|\nabla\phi_1|+\min_{i,j}|\nabla\phi_1|}, \quad \Phi_2 = \dfrac{2|\partial_{\xi\xi} \phi_2|_{i,j}}{\max_{i,j}|\Delta\phi_2|+\min_{i,j}|\Delta\phi_2|}, \quad \Phi_3 = \dfrac{2|\partial_\xi \phi_3|_{i,j}}{\max_{i,j}|\nabla\phi_3|+\min_{i,j}|\nabla\phi_3|}, \\ \Psi_1 = \dfrac{2|\partial_\eta \psi_1|_{i,j}}{\max_{i,j}|\nabla\psi_1|+\min_{i,j}|\nabla\psi_1|}, \quad \Psi_2 = \dfrac{2|\partial_{\eta\eta} \psi_2|_{i,j}}{\max_{i,j}|\Delta\psi_2|+\min_{i,j}|\Delta\psi_2|}, \quad \Psi_3 = \dfrac{2|\partial_\eta \psi_3|_{i,j}}{\max_{i,j}|\nabla\psi_3|+\min_{i,j}|\nabla\psi_3|}, \\ \phi_1 = \phi_2 = \psi_1 = \psi_2 = \rho, \\ \phi_3 = \psi_3 = \rho e - \pi_\infty. \end{cases}$$

Numerical results and CPU time are shown in Fig. 7 and Table 2, respectively. When the adaptive mesh method is used, the mesh points are concentrated at material interface. As a result, the mesh size becomes much smaller and it would take much more CPU time for the adaptive mesh method to simulate. However, a significant improvement in the resolution of solutions can be observed.

Table 2: CPU time comparison.

Mesh type	$N_x \times N_y$	CPU time (second)
Uniform Mesh	70×60	8.5
Moving Mesh	70×60	103.7
Uniform Mesh	420×210	2651.0
Moving Mesh	140×120	1396.6

Table 3: CPU time on uniform mesh.

Mesh type	$N_x \times N_y$	CPU time (second)
Uniform Mesh	105×90	36.2
Uniform Mesh	210×180	310.1
Uniform Mesh	420×210	2651.0

In the second comparison, we are going to show how much acceleration one may expect by using the adaptive mesh method. Note that the computational time is proportional to the number of mesh grids when problems are solved on uniform mesh, which can be clearly seen in Table 3. When the adaptive mesh method is used, the minimum value of the grid size varies step by step, and the CPU time is not easy to estimate. We test the problem on uniform mesh with $N_x \times N_y = 420 \times 360$, and on moving mesh with $N_x \times N_y = 140 \times 120$. Numerical results and CPU time are shown respectively in Fig. 8 and Table 2, from which one can observe that the resolutions of solutions computed on uniform and moving meshes are quite close to each other, but it requires much fewer grid points and takes much less CPU time for the adaptive mesh method to simulate.

In addition to the above two comparisons, one may also see convergence of the adaptive mesh method by comparing solutions on moving meshes with $N_x \times N_y = 70 \times 60$ and $N_x \times N_y = 140 \times 120$.

Interaction of a shock in water with a gas bubble

In the seventh set of tests, the robustness of our approach is illustrated by testing a problem studied in [4,12,45], where an air bubble interacts with a Mach 1.72 shock in water. At the initial state, the bubble is centred at $(x,y)=(6.0,6.0)$ with radius 3.0, and the left-going shock is located at $x=11.4$. Concretely, the initial physical quantities are

$$
\begin{aligned}
&(\rho_1,\rho_2,u,v,p,z_1)\\
=&\begin{cases}
(1.2\times10^{-3},\ 1.325,\ -68.525,\ 0.0,\ 19153.0,\ 10^{-6}), & x>11.4,\\
(1.2\times10^{-3},\ 1.0,\ 0.0,\ 0.0,\ 1.0,\ 1.0-10^{-6}), & d<3.0,\\
(1.2\times10^{-3},\ 1.0,\ 0.0,\ 0.0,\ 1.0,\ 10^{-6}), & \text{elsewhere},
\end{cases}
\end{aligned}
\tag{5.7}
$$

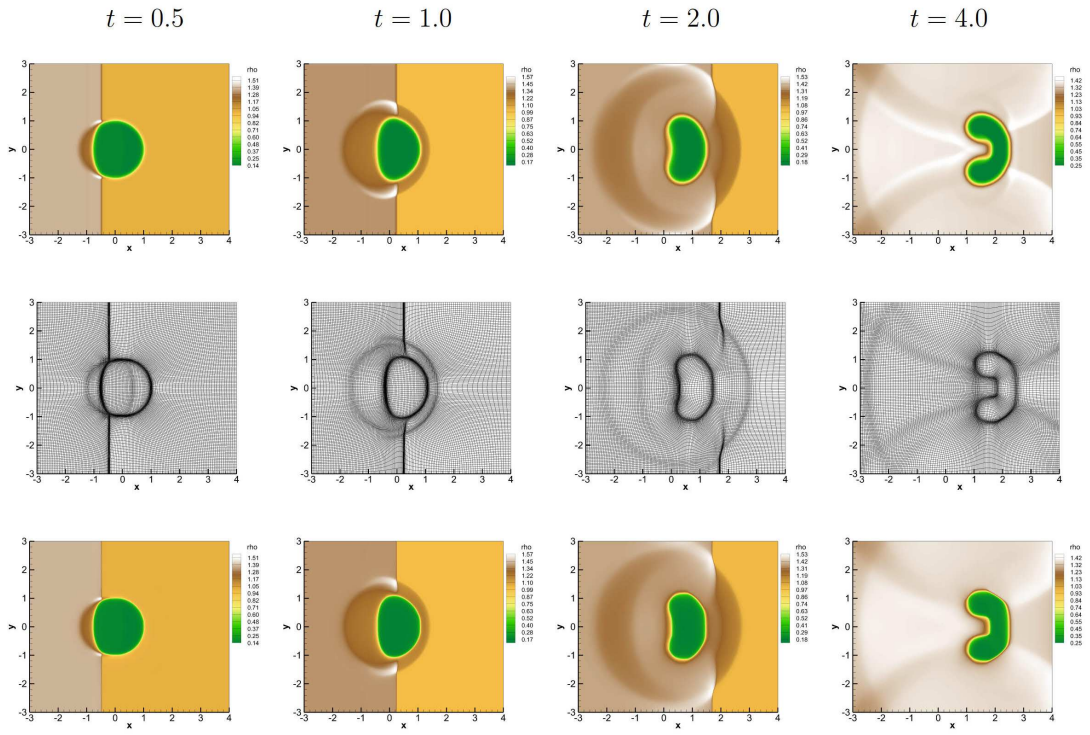

Figure 8: Solutions of an air shock impacting on a helium bubble at multiple output time: $t = 0.5, 1.0, 2.0, 4.0$. Distributions of density computed on uniform mesh (top), with $N_x \times N_y = 420 \times 360$. Distributions of mesh grids (middle) and density on moving mesh (bottom), with $N_x \times N_y = 140 \times 120$.

with $\gamma_1 = 1.4$, $\pi_{\infty,1} = 0.0$ and $\gamma_2 = 4.4$, $\pi_{\infty,2} = 6000.0$, and $d = \sqrt{(x-6)^2+(y-6)^2}$. The problem is computed in $(0,12) \times (0,12)$ with CFL $= 0.9$ until $t = 4.50 \times 10^{-2}$. Transmissive boundary conditions are employed at the left and right boundaries, while reflective boundary conditions are imposed elsewhere.

This problem is challenging since the positivity of the sound speed is difficult to preserve during the whole computation if high order methods are used, and negative sound speed would lead to a crash of the code, as shown in [4]. However, it does not encounter this difficulty when the linear reconstructions together with minmod limiters are used for the primitive variables, since their local extrema are well preserved.

Distributions of the mesh grids and density at multiple output time: $t = 1.02 \times 10^{-2}, 2.04 \times 10^{-2}, 3.05 \times 10^{-2}, 4.05 \times 10^{-2}, 4.50 \times 10^{-2}$, are shown in Fig. 9, where the monitor functions are the same as those for the previous test, except that $\alpha_1 = \alpha_2 = \alpha_3 = 20$. For the solutions computed on the coarse mesh, i.e. under mesh resolution $N_x \times N_y = 100 \times 100$, one can see that the structures of the density has already been produced. However, they are not sharp enough due to lack of the grid points. We also compute the problem with $N_x \times N_y = 500 \times 500$, and find that the solutions are comparable to those presented in [12], where the problem is computed on $N_x \times N_y = 500 \times 500$ uniform mesh by a fifth order al-

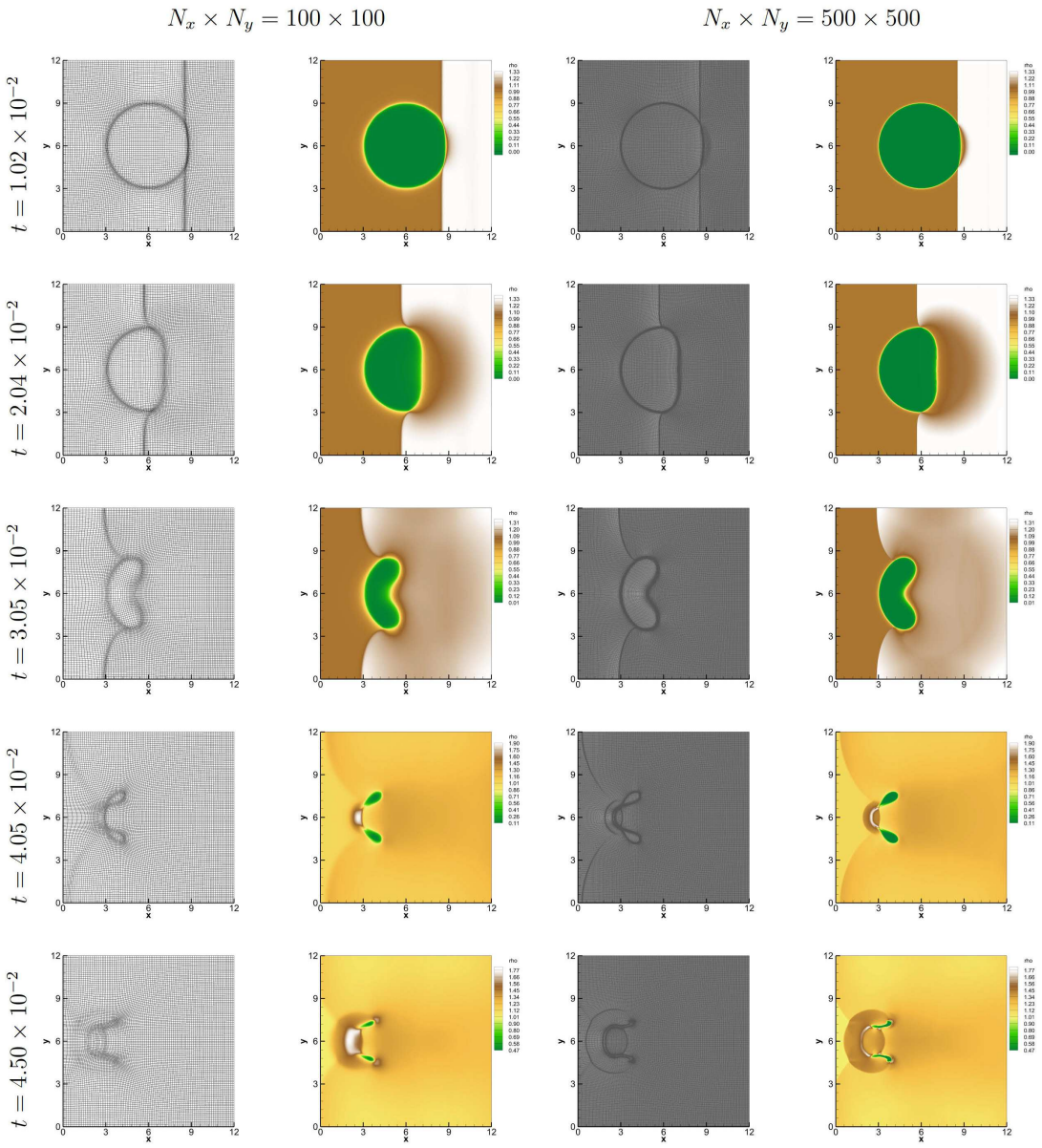

Figure 9: Interaction of a shock in water with a gas bubble: distributions of the mesh grids and density under mesh resolutions $N_x \times N_y = 100 \times 100$ (left two columns) and $N_x \times N_y = 500 \times 500$ (right two columns) at multiple output time: $t = 1.02 \times 10^{-2}, 2.04 \times 10^{-2}, 3.05 \times 10^{-2}, 4.05 \times 10^{-2}, 4.50 \times 10^{-2}$.

ternative WENO scheme with bound- and positivity-preserving limiters. Although our approach only achieves second order of accuracy, it is capable of producing sharp material interface and fine physical structures, since the grid points are suitably concentrated near discontinuities; see the right two columns in Fig. 9. Moreover, it does not require

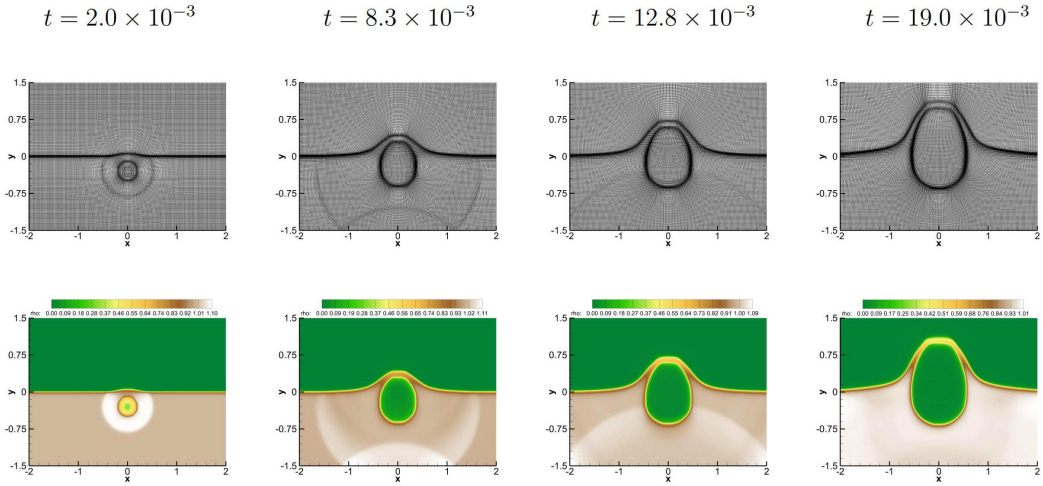

Figure 10: Under water explosion problem: distributions of the mesh grids and density under mesh resolution $N_x \times N_y = 240 \times 180$ at multiple output time: $t = 2.0\times10^{-3}, 8.3\times10^{-3}, 12.8\times10^{-3}, 19.0\times10^{-3}$

.

bound- and positivity-preserving limiters in the simulation, which demonstrates the robustness of the adaptive moving mesh method.

Under water explosion

In the eighth set of tests, the proposed adaptive mesh method is illustrated by simulating the underwater explosion problem studied in [4,7,11,36]. The initial conditions are

$$(\rho_1,\rho_2,u,v,p,z_1) = \begin{cases} (1.225\times10^{-3}, & 1.0, & 0.0, & 0.0, & 1.01325, & 1.0-10^{-10}), & y>0.0, \\ (1.25, & 1.0, & 0.0, & 0.0, & 1.0\times10^{4}, & 1.0-10^{-10}), & d<0.12, \\ (1.25, & 1.0, & 0.0, & 0.0, & 1.01325, & 10^{-10}), & \text{elsewhere}, \end{cases} \tag{5.8}$$

where $\gamma_1 = 1.4$ and $\pi_{\infty,1} = 0.0$ for the air phase; $\gamma_2 = 4.4$ and $\pi_{\infty,1} = 6.0\times10^3$ for the water phase; $d = \sqrt{x^2+(y+0.3)^2}$. The problem is computed in $(-2,2)\times(-1.5,1.5)$ with CFL $=$ 0.9. Reflective boundary conditions are imposed at the top and bottom boundaries, while transmissive boundary conditions are employed elsewhere.

Numerical solutions are shown in Fig. 10 where distributions of the mesh grids and density are plotted under mesh resolution $N_x \times N_y = 240\times180$ at multiple output time: $t=2.0\times10^{-3}, 8.3\times10^{-3}, 12.8\times10^{-3}, 19.0\times10^{-3}$. In this test, we have used the same monitor functions as those for the previous test. From the figure, one may clearly observe that distributions of the grid points are concentrated near the material interface and shocks at every output time, which in turn provides high resolution solutions, such as the air bubble which evolves from a circle to oval-like shapes.

6 Conclusions

In this paper, a second order finite volume discretization with minmod limiter is proposed for the five-equation model, where we have slightly modified the advection equation for the volume fraction. This serves as the first ingredient of our approach. Meanwhile, adaptive moving mesh method is applied as the second ingredient to improve the numerical resolution of the solutions. Besides, we have also proved that the proposed approach preserves the E-property. Numerical examples illustrate that the E-property is preserved and the physical structures, such as the rarefaction wave, material interface and shock wave, are perfectly resolved. Moreover, challenging test problems have demonstrated the effectiveness and robustness of our approach.

Acknowledgments

The research of Yaguang Gu is funded by China Postdoctoral Science Foundation (2021M703040). The research of Dongmi Luo is supported by the National Natural Science Foundation of China (12101063). The research of Zhen Gao is supported by the National Natural Science Foundation of China (11871443), Shandong Provincial Qingchuang Science and Technology Project (2019KJI002) and Fundamental Research Funds for the Central Universities (202042004). The research of Yibing Chen is supported by National Key Project (GJXM92579).

References

[1] G. Allaire, S. Clerc, and S. Kokh, *A five-equation model for the simulation of interfaces between compressible fluids*, Journal of Computational Physics, 181 (2002), pp. 577–616.

[2] T. D. Aslam, J. B. Bdzil, and D. S. Stewart, *Level set methods applied to modeling detonation shock dynamics*, Journal of Computational Physics, 126 (1996), pp. 390–409.

[3] J. Cheng and C.-W. Shu, *Positivity-preserving Lagrangian scheme for multi-material compressible flow*, Journal of Computational Physics, 257 (2014), pp. 143–168.

[4] J. Cheng, F. Zhang, and T. Liu, *A quasi-conservative discontinuous Galerkin method for solving five equation model of compressible two-medium flows*, Journal of Scientific Computing, 85:12 (2020).

[5] V. Coralic and T. Colonius, *Finite-volume WENO scheme for viscous compressible multicomponent flows*, Journal of Computational Physics, 274 (2014), pp. 95–121.

[6] M. J. Del Razo and R. J. LeVeque, *Numerical methods for interface coupling of compressible and almost incompressible media*, SIAM Journal on Scientific Computing, 39 (2017), pp. B486–B507.

[7] X. Deng, S. Inaba, B. Xie, K.-M. Shyue, and F. Xiao, *High fidelity discontinuity-resolving reconstruction for compressible multiphase flows with moving interfaces*, Journal of Computational Physics, 371 (2018), pp. 945–966.

[8] R. P. Fedkiw, T. Aslam, B. Merriman, and S. Osher, *A non-oscillatory Eulerian approach to interfaces in multimaterial flows (the ghost fluid method)*, Journal of Computational Physics, 152 (1999), pp. 457–492.

[9] J. GLIMM, J. W. GROVE, X. L. LI, K.-M. SHYUE, Y. ZENG, AND Q. ZHANG, *Three-dimensional front tracking*, SIAM Journal on Scientific Computing, 19 (1998), pp. 703–727.
[10] L. D. GRYNGARTEN AND S. MENON, *A generalized approach for sub- and super-critical flows using the local discontinuous Galerkin method*, Computer Methods in Applied Mechanics and Engineering, 253 (2013), pp. 169–185.
[11] Y. GU, Z. GAO, G. HU, P. LI, AND L. WANG, *High order finite difference alternative WENO scheme for multi-component flows*, 89:52 (2021).
[12] ——, *A robust high order alternative WENO scheme for the five-equation model*, Journal of Scientific Computing, 88:12 (2021).
[13] Y. GU AND G. HU, *A third order adaptive ADER scheme for one dimensional conservation laws*, Communications in Computational Physics, 22 (2017), pp. 829–851.
[14] P. HE AND H. TANG, *An adaptive moving mesh method for two-dimensional relativistic hydrodynamics*, Communications in Computational Physics, 11 (2012), pp. 114–146.
[15] ——, *An adaptive moving mesh method for two-dimensional relativistic magnetohydrodynamics*, Computers & Fluids, 60 (2012), pp. 1–20.
[16] C. HIRT, A. AMSDEN, AND J. COOK, *An arbitrary Lagrangian-Eulerian computing method for all flow speeds*, Journal of Computational Physics, 14 (1974), pp. 227–253.
[17] G. HU, *An adaptive finite volume method for 2D steady Euler equations with WENO reconstruction*, Journal of Computational Physics, 252 (2013), pp. 591–605.
[18] G. HU, X. MENG, AND N. YI, *Adjoint-based an adaptive finite volume method for steady Euler equations with non-oscillatory k-exact reconstruction*, Computers & Fluids, 139 (2016), pp. 174–183.
[19] G. HU AND N. YI, *An adaptive finite volume solver for steady Euler equations with non-oscillatory k-exact reconstruction*, Journal of Computational Physics, 312 (2016), pp. 235–251.
[20] W. HUANG AND R. D. RUSSELL, *Adaptive Moving Mesh Methods*, Springer-Verlag New York, 2011.
[21] E. JOHNSEN AND T. COLONIUS, *Implementation of WENO schemes in compressible multicomponent flow problem*, Journal of Computational Physics, 219 (2006), pp. 715–732.
[22] A. KURGANOV, Z. QU, O. S. ROZANOVA, AND T. WU, *Adaptive moving mesh central-upwind schemes for hyperbolic system of PDEs: Applications to compressible Euler equations and granular hydrodynamics*, Communications on Applied Mathematics and Computation, (2020).
[23] R. J. LEVEQUE, *Finite Volume Methods for Hyperbolic Problems*, Cambridge University Press, 2002.
[24] R. LI, *On multi-mesh h-adaptive methods*, Journal of Scientific Computing, 24 (2005), pp. 321–341.
[25] R. LI AND T. TANG, *Moving mesh discontinuous Galerkin method for hyperbolic conservation laws*, Journal of Scientific Computing, 27 (2006), pp. 347–363.
[26] R. LI, X. WANG, AND W. ZHAO, *A multigrid block LU-SGS algorithm for Euler equations on unstructured grids*, Numerical Mathematics: Theory, Methods and Applications, 1 (2008), pp. 92–112.
[27] D. LUO, W. HUANG, AND J. QIU, *A quasi-Lagrangian moving mesh discontinuous Galerkin method for hyperbolic conservation laws*, Journal of Computational Physics, 396 (2019), pp. 544–578.
[28] D. LUO, S. LI, W. HUANG, J. QIU, AND Y. CHEN, *A quasi-conservative DG-ALE method for multi-component flows using the non-oscillatory kinetic flux*, 2021. Submitted, arXiv: 2101.04897.
[29] D. LUO, J. QIU, J. ZHU, AND Y. CHEN, *A quasi-conservative discontinuous Galerkin method for multi-component flows using the non-oscillatory kinetic flux*, Journal of Scientific Computing,

87:96 (2021).
[30] S. OSHER AND J. SETHIAN, *Fronts propagating with curvature-dependent speed: Algorithms based on Hamilton-Jacobi formulations*, Journal of Computational Physics, 79 (1988), pp. 12–49.
[31] J. QIU, T. LIU, AND B. C. KHOO, *Simulations of compressible two-medium flow by Runge-Kutta discontinuous Galerkin methods with the ghost fluid method*, Communications in Computational Physics, 3 (2008), pp. 479–504.
[32] R. SAUREL AND R. ABGRALL, *A simple method for compressible multifluid flows*, SIAM Journal on Scientific Computing, 21 (1999), pp. 1115–1145.
[33] ——, *A simple method for compressible multifluid flows*, SIAM Journal on Scientific Computing, 21 (1999), pp. 1115–1145.
[34] R. SAUREL AND C. PANTANO, *Diffuse-interface capturing methods for compressible two-phase flows*, Annual Review of Fluid Mechanics, 50 (2018), pp. 105–130.
[35] C.-W. SHU AND S. OSHER, *Efficient implementation of essentially non-oscillatory shock-capturing schemes*, Journal of Computational Physics, 77 (1988), pp. 439–471.
[36] R. K. SHUKLA, C. PANTANO, AND J. B. FREUND, *An interface capturing method for the simulation of multi-phase compressible flows*, Journal of Computational Physics, 229 (2010), pp. 7411–7439.
[37] K.-M. SHYUE, *An efficient shock-capturing algorithm for compressible multicomponent problems*, Journal of Computational Physics, 142 (1998), pp. 208–242.
[38] H. TANG AND T. TANG, *Adaptive mesh methods for one- and two-dimensional hyperbolic conservation laws*, SIAM Journal on Numerical Analysis, 41 (2003), pp. 487–515.
[39] E. F. TORO, *Riemann Solvers and Numerical Methods for Fluid Dynamics: A Practical Introduction*, Springer-Verlag Berlin Heidelberg, 2009.
[40] R. VERFÜRTH, *A Posteriori Error Estimation Techniques for Finite Element Methods*, Oxford University Press, 2013.
[41] F. VILAR, C.-W. SHU, AND P.-H. MAIRE, *Positivity-preserving cell-centered Lagrangian schemes for multi-material compressible flows: From first-order to high-orders. Part I: The one-dimensional case*, Journal of Computational Physics, 312 (2016), pp. 385–415.
[42] J. VON NEUMANN AND R. RICHTMYER, *A method for the numerical calculation of hydrodynamic shocks*, Journal of Applied Physics, 21 (1950), pp. 232–237.
[43] A. M. WINSLOW, *Numerical solution of the quasilinear poisson equation in a nonuniform triangle mesh*, Journal of Computational Physics, 1 (1966), pp. 149–172.
[44] M. L. WONG, J. B. ANGEL, M. F. BARAD, AND C. C. KIRIS, *A positivity-preserving high-order weighted compact nonlinear scheme for compressible gas-liquid flows*, Journal of Computational Physics, 444 (2021), p. 110569.
[45] L. XU AND T. LIU, *Explicit interface treatments for compressible gas-liquid simulations*, Computers & Fluids, 153 (2017), pp. 34–48.
[46] X. YANG, W. HUANG, AND J. QIU, *A moving mesh WENO method for one-dimensional conservation laws*, SIAM Journal on Scientific Computing, 34 (2012), pp. A2317–A2343.
[47] C. ZHANG AND I. MENSHOV, *Using the composite Riemann problem solution for capturing interfaces in compressible two-phase flows*, Applied Mathematics and Computation, 363:15 (2019).
[48] Z. ZHAO, Y. CHEN, AND J. QIU, *A hybrid WENO method with modified ghost fluid method for compressible two-medium flow problems*, Numerical Mathematics: Theory, Methods and Applications, 14 (2021), pp. 972–997.